Model of Propagation of VLF Beams in the Waveguide Earth-Ionosphere. Principles of Tensor Impedance Method in Multilayered Gyrotropic Waveguides.

Yuriy Rapoport[#±1], Vladimir Grimalsky[*2], Victor Fedun[~3], Oleksiy Agapitov [#⊥4], John Bonnell[⊥5], Asen Grytsai[#6], Gennadi Milinevsky[#ε7], Alex Liashchuk[±8], Alexander Rozhnoi[φ9], Maria Solovieva[φ10], Andrey Gulin[#11]

[#]Taras Shevchenko National University of Kyiv, Ukraine
[*]Autonomous University of State Morelos (UAEM), Mexico
[~]The University of Sheffield, UK
[⊥]University of California, Berkeley, USA
[ε]College of Physics, International Center of Future Science, Jilin University, Changchun, China
[±] National Space Facilities Control and Test Center, State Space Agency of Ukraine
[φ]Institute of the Earth Physics, RAS, Moscow, Russia

[1]yuriy.rapoport@gmail.com, [2]v_grim@yahoo.com, [3]v.fedun@sheffield.ac.uk, [4]oleksiy.agapitov@gmail.com, [5]jwbonnell@berkeley.edu, [6]a.grytsai@gmail.com, [7]genmilinevsky@gmail.com, [8]alex.liashchukk@gmail.com, [9]rozhnoi@ifz.ru, [10]MCSolovieva@gmail.com, [11]mytimetosay@gmail.com

Correspondence to: Yuriy Rapoport (yuriy.rapoport@gmail.com)_

Abstract. The modeling of very low frequency electromagnetic beam propagation in the earth-ionosphere waveguide is considered. A new tensor impedance method for modeling propagation of electromagnetic beams in a multi-layered/inhomogeneous waveguide is presented. The waveguide is assumed to possess the gyrotropy and inhomogeneity with a thick cover layer placed above the waveguide. The influence of geomagnetic field inclination and carrier beam frequency on the characteristics of the polarization transformation in the Earth-ionosphere waveguide is determined. The new method for modeling of propagation of electromagnetic beams allows us to study: (i) propagation of the very low frequency modes in the earth-ionosphere waveguide and, in perspective, their excitation by the typical Earth-ionosphere waveguide sources, such as radio wave transmitters and lightning discharges and (ii) leakage of Earth-ionosphere waveguide waves into the upper ionosphere/magnetosphere. The proposed approach can be applied to the variety of problems related to the analysis of propagation of electromagnetic waves in layered gyrotropic/anisotropic active media in a wide frequency range, e.g. from the Earth-ionosphere waveguide to optics waveband, an artificial signal propagation such as metamaterial microwave or optical waveguides.

Keywords — ionosphere, atmosphere, VLF, tensor impedance, gyrotropy, layered waveguide, beam, electromagnetic waves, boundary conditions, ionospheric disturbances, vertical coupling processes

1 Introduction

The results of analytical and numerical study of very low frequency (VLF) electromagnetic (EM) wave/beam propagation in the Lithosphere–Atmosphere–Ionosphere–Magnetosphere system (LAIM), in particular in the waveguide "Earth-Ionosphere" (WGEI) are presented. The amplitude and phase of the VLF wave propagates in the earth-ionosphere waveguide (WGEI) can change, and these changes may be observable using ground-based and/or satellite detectors. This reflects the

variations in the ionospheric electrodynamic characteristics (complex dielectric permittivity) and the influences on the ionosphere, for example, "from above" by chain Sun – Solar Wind – Magnetosphere – Ionosphere (Patra et al., 2011; Koskinen, 2011; Boudjada et al., 2012; Wu et al., 2016; Yiğit et al., 2016). Then the influence on the ionosphere "from below" comes from the most powerful meteorological, seismogenic and other sources in the lower atmosphere and lithosphere/Earth, such as cyclones and hurricanes (Nina et al., 2017; Rozhnoi et al., 2014; Chou et al., 2015) as well as from earthquakes (Hayakawa, 2015; Surkov and Hayakawa, 2014; Sanchez-Dulcet et al., 2015) and tsunamis. From inside the ionosphere the strong thunderstorms, lightning discharges, and terrestrial gamma-ray flashes or sprite streamers (Cummer et al., 1998; Qin et al., 2012; Dwyer, 2012; Dwyer and Uman, 2014; Cummer et al., 2014; Mezentsev et al., 2018) influence the ionospheric electrodynamic characteristics as well. Note that the VLF signals are very important for the merging of the atmospheric physics and space plasma physics with astrophysics and high-energy physics. The corresponding "intersection area" for these four disciplines includes cosmic rays and very popular now objects of investigation – high-altitude discharges (sprites), anomalous X-ray bursts, and powerful gamma-ray bursts. The key phenomena for the occurrence of all of these objects is the appearance of runaway avalanche in the presence of high energy seed electrons. In the atmosphere, there are cosmic ray secondary electrons (Gurevich and Zybin, 2001). Consequently, these phenomena are intensified during the air shower generating by cosmic particles (Gurevich and Zybin, 2001; Gurevich et al., 2009). The runaway breakdown and lightning discharges including **high-altitude** ones can **cause** radio emission both in HF range, which could be observed using the Low-Frequency Array (LOFAR) radio telescope network facility and other radio telescopes (Buitink et al., 2014; Scholten et al., 2017; Hare et al., 2018), and in the VLF range (Gurevich and Zybin, 2001). The corresponding experimental research includes the measurements of the VLF characteristics by the international measurement system of the pairs "transmitted-receiver" separated by a distance of a couple of thousand km (Biagi et al., 2011; 2015). The World Wide Lightning Location Network is the one more international facility for VLF measurements during thunderstorms with lightning discharges (Lu et al. 2019)**.** Intensification of magnetospheric research, wave processes, particle distribution and wave-particle interaction in the magnetosphere including radiation belts leads to the great interest to the VLF plasma waves, in particular whistlers (Artemyev et al., 2013, 2015; Agapitov et al., 2014; Agapitov et al., 2018)**.**

The differences of the proposed model for the simulation of VLF waves in the WGEI from others can be summarized in three main points. (i) In distinction to the impedance invariant imbedding model (Shalashov and Gospodchikov, 2010; Kim and Kim, 2016), our model provides an optimal balance between the analytical and numerical approaches. It combines analytical-numerical approaches basing on matrix sweep method (Samarskii, 2001). As a result, this model allows to obtain analytically the tensor impedance and, at the same time, provides high effectiveness and stability of the modeling. (ii) In distinction to the full-wave finite difference time domain models (Chevalier and Inan, 2006; Marshall et al., 2017; Yu et al., 2012; Azadifar et al., 2017), our method provides the physically clear lower and upper boundary conditions, in particular physically justified upper boundary conditions corresponding to the radiation of the waves propagation in the WGEI to the upper ionosphere/magnetosphere. This allows to determine the leakage modes and to interpret not only ground-based, but also satellite measurements of the VLF beam characteristics. (iii) In distinction to the

models considered in (Kuzichev and Shklyar, 2010; Kuzichev et al., 2018; Lehtinen and Inan, 2009; Lehtinen and Inan, 2008) based on the mode presentations and made in the frequency domain, we use the combined approach. This approach includes the radiation condition at the altitudes of the F-region, equivalent impedance conditions in the lower E-region and at the lower boundary of the WGEI, mode approach, and finally, the beam method. This combined approach, finally, creates the possibility to interpret adequately data of both ground-based and satellite detection on the VLF EM wave/beam propagating in the WGEI and those, which experienced a leakage from the WGEI into the upper ionosphere and magnetosphere. Some other details on the distinctions from the previously published models are given below in Sect. 3.

The methods of effective boundary conditions such as effective impedance conditions (Tretyakov, 2003; Senior and Volakis, 1995; Kurushin and Nefedov, 1983) are well-known and can be used, in particular, for the layered metal-dielectric, metamaterial and gyrotropic active layered and waveguiding media of different types (Tretyakov, 2003; Senior and Volakis, 1995; Kurushin and Nefedov, 1983; Collin, 2001; Wait, 1996) including plasma-like solid state (Ruibys, and Tolutis, 1983) and space plasma (Wait, 1996) media. The plasma wave processes in the waveguide structures metal-semiconductor-dielectric, placed into the external magnetic field, were widely investigated (Ruibys and Tolutis, 1983; Maier, 2007; Tarkhanyan and Uzunoglu, 2006) from radio to optical frequency ranges. Corresponding waves are applied in modern plasmonics and in non-destructive testing of semiconductor interfaces. It is interesting to realize the resonant interactions of volume and surface electromagnetic waves in these structures, so the simulations of the wave spectrum are important. To describe such complex layered structures, it is very convenient and effective to use impedance approach (Tretyakov, 2003; Senior and Volakis, 1995; Kurushin and Nefedov, 1983). As a rule, impedance boundary conditions are used, when the layer covering waveguide is thin (Senior and Volakis, 1995; Kurushin and Nefedov, 1983). One of the known exclusions is the impedance invariant imbedding model. The difference between our new method and that model is already mentioned above and is explained in more details in the Subsection 3.3. Our new approach, i.e a new tensor impedance method for modeling propagation of electromagnetic beams (TIMEB), includes a set of very attractive features for practical purposes. These features are: (i) the surface impedance characterizes cover layer of finite thickness, and this impedance is expressed analytically; (ii) the method allows an effective modelling of 3D beam propagating in the gyrotropic waveguiding structure; (iii) finally, if the considered waveguide can be modified by any external influence such as bias magnetic or electric fields, or by any extra wave or energy beams (such as acoustic or quasistatic fields etc.), the corresponding modification of the characteristics (phase and amplitude) of the VLF beam propagating in the waveguide structure can be modelled.

Our approach was targeting properly and is suitable for the further development which will allow to solve also the following problems: (i) the problem of the excitation of the waveguide by the waves incident on the considered structure from above could be solved as well with the slight modification of the presented model, with inclusion also ingoing waves; (ii) to consider a plasma-like system placed into the external magnetic field, such as the LAIM system (Grimalsky et al., 1999 a, b) or dielectric-magnetized semiconductor structure. The electromagnetic waves radiated outside the waveguiding structure, such as helicons (Ruibys and Tolutis, 1983) or whistlers (Wait, 1996), and the waveguide modes could be considered altogether. An adequate boundary radiation conditions on the upper boundary of the covering layer are derived.

3

104 Based on this and absence of ingoing waves, the leakage modes above the upper boundary of the structure (in other words,
105 upper boundary of covering layer), will be searched with the further development of the model delivered in the present
106 paper. Namely, it will be possible to investigate the process of the leakage of electromagnetic waves from the open
107 waveguide. Then their transformation into magnetized plasma waves, propagating along magnetic field lines, and the
108 following excitation of the waveguiding modes by the waves incident on the system from external space (Walker, 1976), can
109 be modeled as a whole. Combining with the proper measurements of the phases and amplitudes of the electromagnetic
110 waves, propagating in the waveguiding structures and leakage waves, the model can be used for searching, and even
111 monitoring the external influences on the layered gyrotropic active artificial or natural media, for example, microwave or
112 optical waveguides or the system LAIM and the earth-ionosphere waveguide, respectively.

113 An important effect of the gyrotropy and anisotropy is the corresponding transformation of the field polarization
114 during the propagation in the WGEI, absent in the ideal metal planar waveguide without gyrotropy and anisotropy. We will
115 search, how such an effect depends on the carrier frequency of the beam, propagating in the WGEI, inclination of the
116 geomagnetic field and perturbations in the electron concentration, which could vary under the influences of the powerful
117 enough sources placed "below", "above" and/or "inside" the ionosphere.

118 In Sect. 2 formulation of the problem is presented. In Sect. 3 the algorithm is discussed including the determination
119 of the VLF waves/beams radiation conditions into the upper ionosphere/magnetosphere at the upper boundary, placed in the
120 F-region at the altitude (250-400) km. The effective tensor impedance boundary conditions at the upper boundary (~ 85 km)
121 of the effective earth-ionosphere waveguide and the 3D model TIMEB of the propagation of the VLF beam in the WGEI are
122 discussed as well. The issues regarding the VLF beam leakage regimes are considered only very briefly, since the relevant
123 details will be presented in the following articles. In Sect. 4 the results of the numerical modeling are presented. In Sect. 5
124 the discussion is presented, including an example of the qualitative comparison between the results of our theory and an
125 experiment including the future rocket experiment on the measurements of the characteristics of VLF signal radiated from
126 the artificial VLF transmitter, which is propagating in the WGEI and penetrating into the upper ionosphere.

127

128 **2 Formulation of the problem**

129

130 The VLF electromagnetic (EM) waves with frequencies $f = (10 - 100)$ kHz can propagate along the Earth's surface for long
131 distances >1000 km. The Earth's surface of a high conductivity z = 0 (z is vertical coordinate) and the ionosphere F-layer z
132 = 300 km form the VLF waveguide, see Fig. 1. The propagation of the VLF electromagnetic radiation excited by a near-
133 Earth antenna within the WGEI should be described by the full set of Maxwell's equations in the isotropic atmosphere $0 < z$
134 < 60 km, the approximately isotropic ionosphere D-layer 60 km $< z < 75$ km, and the anisotropic E- and F- layers of the
135 ionosphere, due to the geomagnetic field $\vec{H}_0$, added by the boundary conditions at the Earth's surface and at the F-layer. In
136 Fig. 1, θ is the angle between the directions of the vertical axis z and geomagnetic field $\vec{H}_0$. Note that theta θ angle is

137 complementary to the angle of inclination of the geomagnetic field. Geomagnetic field $\vec{H}_0$ is directed along z' axis, lies in

138 the plane xz, while the planes $x'z'$ and xz coincide with each other.

139

140
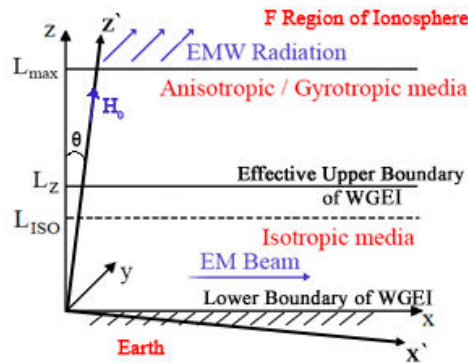
Figure 1. The geometry of the anisotropic/gyrotropic waveguide. EM waves propagate in OX direction. $\vec{H}_0$ is the external magnetic field. The effective WGEI for EM waves occupies the region $0 < z < L_z$. The isotropic medium occupies the region $0 < z < L_{ISO}$, $L_{ISO} < L_z$. The anisotropic/gyrotropic medium occupies the region $L_{ISO} < z < L_{max}$. Covering layer occupies the region $L_z < z < L_{max}$. WG includes isotropic region $0 < z < L_{ISO}$ and a part of anisotropic region $L_z < z < L_{max}$. It is supposed that the anisotropic region is relatively small part of the WG, $(L_z-L_{ISO})/L_z \sim (0.1\text{-}0.2)$. At the upper boundary of covering layer ($z = L_{max}$) the radiation of EM to the external region ($z > L_{max}$) is accounted for with the proper boundary conditions. Integration of the equations describing the EM field propagation allows to obtain effective impedance boundary conditions at the upper boundary of effective WG ($z = L_z$). These boundary conditions effectively includes all the effects on the wave propagation of the covering layer and the radiation (at $z = L_{max}$) to the external region ($z > L_{max}$).

150

151 **3. Algorithm**

152 The boundary conditions and calculations of impedance and beam propagation in the WGEI is considered in this Secion. The

153 other parts of the algorithm, e.g. the reflection of the EM waves from the WGEI effective upper boundary and the leakage of

154 EM waves from the WGEI to the upper ionosphere/magnetosphere, will be presented very briefly as they are the subjects of

155 the next papers.

3.1 Direct and inverse tensors characterizing the ionosphere

157 In the next subsections we derived the formulas describing the transfer of the boundary conditions at the upper boundary ($z =$

158 L_{max}), Fig. 1, resulting in the tensor impedance conditions at the upper boundary of the effective WGEI ($z = L_i$). Firstly let's

159 describe the tensors characterizing the ionosphere.

160 The algorithm's main goal is to transfer the EM boundary conditions from the upper ionosphere at the height $L_z \sim 250 - 400$

161 km to the lower ionosphere $L_z \sim 70 - 90$ km. All components of the monochromatic EM field is considered to be

162 proportional to exp*(iωt)*. The anisotropic medium is inhomogeneous along *OZ* axis only and characterized by the

163 permittivity tensor $\hat{\varepsilon}(\omega, z)$ or by the inverse tensor $\hat{\beta}(\omega, z) = \hat{\varepsilon}^{-1}(\omega, z)$: $\vec{E} = \hat{\beta}(\omega, z) \cdot \vec{D}$, where $\vec{D}$ is the electric induction.

164 Below the absolute units are used. The expressions for the components of the effective permittivity of the ionosphere are in

165 the coordinate frame X'YZ' where OZ' axis is aligned along the geomagnetic field $\vec{H}_0$:

166

$$\hat{\varepsilon}' = \begin{pmatrix} \varepsilon_1 & \varepsilon_h & 0 \\ -\varepsilon_h & \varepsilon_1 & 0 \\ 0 & 0 & \varepsilon_3 \end{pmatrix}, \quad \varepsilon_1 = 1 - \frac{\omega_{pe}^2 \cdot (\omega - i\nu_e)}{((\omega - i\nu_e)^2 - \omega_{He}^2) \cdot \omega} - \frac{\omega_{pi}^2 \cdot (\omega - i\nu_i)}{((\omega - i\nu_i)^2 - \omega_{Hi}^2) \cdot \omega}, \quad \varepsilon_h \equiv ig;$$

167
$$g = -\frac{\omega_{pe}^2 \cdot \omega_{He}}{((\omega - i\nu_e)^2 - \omega_{He}^2) \cdot \omega} + \frac{\omega_{pi}^2 \cdot \omega_{Hi}}{((\omega - i\nu_i)^2 - \omega_{Hi}^2) \cdot \omega}, \quad \varepsilon_3 = 1 - \frac{\omega_{pe}^2}{(\omega - i\nu_e) \cdot \omega} - \frac{\omega_{pi}^2}{(\omega - i\nu_i) \cdot \omega};$$ (1)

$$\omega_{pe}^2 = \frac{4\pi e^2 n}{m_e}, \quad \omega_{pi}^2 = \frac{4\pi e^2 n}{m_i}, \quad \omega_{He} = \frac{eH_0}{m_e c}, \quad \omega_{Hi} = \frac{eH_0}{m_i c}$$

168

169 Here $\omega_{pe}, \omega_{pi}, \omega_{He}, \omega_{Hi}$ are the plasma and cyclotron frequencies for electrons and ions, respectively; m_e, m_i, ν_e, ν_i are the

170 masses and collision frequencies for electrons and ions, respectively, n is electron concentration. The approximations of

171 the three-component plasma-like ionosphere (including electron, one effective ion and one effective neutral

172 components) and quasi-neutrality are accepted. The expressions for the components of permittivity tensor $\hat{\varepsilon}(\omega, z)$ are

173 obtained from (1) by means of multiplication with the standard rotation matrices (Spiegel, 1959) dependent on angle θ. For

174 the medium with a scalar conductivity σ, e.g. lower ionosphere or atmosphere, the effective permittivity in (1) reduces to $\varepsilon =$

175 1 - $4\pi i\sigma/\omega$.

3.2 The equations for the EM field and upper boundary conditions

177 The case of the VLF waveguide modes k_x is slightly complex and should be calculated accounting for boundary conditions at

178 the Earth's surface and upper surface of the effective WGEI. The EM field depends on the horizontal coordinate x as

179 exp(-$k_x x$). Taking into account $k_x \leq k_0$ ($k_0 = \omega/c$), in simulations of the VLF beam propagation, we assume $k_x = k_0$.

180 Therefore, Maxwell's equations are:

$$-\frac{\partial H_y}{\partial z} = ik_0 D_x, \quad \frac{\partial H_x}{\partial z} + ik_x H_z = ik_0 D_y, \quad -ik_x H_y = ik_0 D_z$$

181
$$-\frac{\partial E_y}{\partial z} = -ik_0 H_x, \quad \frac{\partial E_x}{\partial z} + ik_x E_z = -ik_0 H_y, \quad -ik_x E_y = -ik_0 H_z$$ (2)

182 Here, $E_x = \beta_{11} D_x + \beta_{12} D_y + \beta_{13} D_z$ etc. All components of the EM field can be represented through the horizontal components

183 of the magnetic field H_x, and H_y. The equations for these components are:

6

184

$$\frac{\partial}{\partial z}\left(\frac{\beta_{22}}{1-\beta_{22}\frac{k_x^2}{k_0^2}}\frac{\partial H_x}{\partial z}\right)-\frac{\partial}{\partial z}\left(\frac{\beta_{21}}{1-\beta_{22}\frac{k_x^2}{k_0^2}}\frac{\partial H_y}{\partial z}\right)-ik_x\frac{\partial}{\partial z}\left(\frac{\beta_{23}}{1-\beta_{22}\frac{k_x^2}{k_0^2}}H_y\right)+k_0^2H_x=0 \tag{3a}$$

185

$$\frac{\partial}{\partial z}\left((\beta_{11}+\frac{k_x^2}{k_0^2}\frac{\beta_{12}\cdot\beta_{21}}{1-\beta_{22}\frac{k_x^2}{k_0^2}})\frac{\partial H_y}{\partial z}\right)-\frac{\partial}{\partial z}\left(\frac{\beta_{12}}{1-\beta_{22}\frac{k_x^2}{k_0^2}}\frac{\partial H_x}{\partial z}\right)+$$

$$+ik_x\frac{\partial}{\partial z}\left((\beta_{13}+\frac{k_x^2}{k_0^2}\frac{\beta_{12}\cdot\beta_{23}}{1-\beta_{22}\frac{k_x^2}{k_0^2}})H_y\right)+ik_x(\beta_{31}+\frac{k_x^2}{k_0^2}\frac{\beta_{32}\cdot\beta_{21}}{1-\beta_{22}\frac{k_x^2}{k_0^2}})\frac{\partial H_y}{\partial z}- \tag{3b}$$

$$-ik_x\frac{\beta_{32}}{1-\beta_{22}\frac{k_x^2}{k_0^2}}\frac{\partial H_x}{\partial z}+k_0^2(1-\beta_{33}\frac{k_x^2}{k_0^2}-\frac{k_x^4}{k_0^4}\frac{\beta_{23}\cdot\beta_{32}}{1-\beta_{22}\frac{k_x^2}{k_0^2}})H_y=0$$

186 The expressions for the horizontal components of the electric field E_x, E_y are:

187

$$E_x=\frac{i}{k_0}\left((\beta_{11}+\frac{k_x^2}{k_0^2}\frac{\beta_{12}\cdot\beta_{21}}{1-\beta_{22}\frac{k_x^2}{k_0^2}})\frac{\partial H_y}{\partial z}-\frac{\beta_{12}}{1-\beta_{22}\frac{k_x^2}{k_0^2}}\frac{\partial H_x}{\partial z}\right)-\frac{k_x}{k_0}(\beta_{13}+\frac{k_x^2}{k_0^2}\frac{\beta_{12}\cdot\beta_{23}}{1-\beta_{22}\frac{k_x^2}{k_0^2}})H_y$$

188

$$E_y=\frac{i}{k_0}\left(-\frac{\beta_{22}}{1-\beta_{22}\frac{k_x^2}{k_0^2}}\frac{\partial H_x}{\partial z}+\frac{\beta_{21}}{1-\beta_{22}\frac{k_x^2}{k_0^2}}\frac{\partial H_y}{\partial z}\right)-\frac{k_x}{k_0}\frac{\beta_{23}}{1-\beta_{22}\frac{k_x^2}{k_0^2}}H_y \tag{4}$$

189 In the region $z \geq L_{max}$ the upper ionosphere is assumed to be weakly inhomogeneous, and the geometric optics approximation

190 is valid in the VLF range there. We should note that due to high inhomogeneity of the ionosphere in the vertical direction

191 within E-layer (i.e. at the upper boundary of the effective VLF WGEI) such an approximation is not applicable. These

192 conditions determine the choice of the upper boundary $z = L_{max} \sim (250 - 400)$ km, where the conditions of the radiation are

193 formulated. The dispersion equation connected the wave numbers and the frequency of the outgoing waves is obtained from

194 Eqs. (3), where $H_{x,y} \sim \exp(-ik_z\tilde{z})$, while the derivatives like $\partial\beta_{11}/\partial z$ and the inhomogeneity of the media are neglected:

7

$$\left(\beta_{22}k_z^2 - k_0^2(1-\beta_{22}\frac{k_x^2}{k_0^2})\right)\cdot\left((\beta_{11}(1-\beta_{22}\frac{k_x^2}{k_0^2})+\frac{k_x^2}{k_0^2}\beta_{12}\cdot\beta_{21})k_z^2 + ((\beta_{13}+\beta_{31})(1-\beta_{22}\frac{k_x^2}{k_0^2})+\right.$$

$$+\frac{k_x^2}{k_0^2}(\beta_{12}\cdot\beta_{23}+\beta_{32}\cdot\beta_{21})k_xk_z - k_0^2((1-\beta_{33}\frac{k_x^2}{k_0^2})(1-\beta_{22}\frac{k_x^2}{k_0^2})-\frac{k_x^4}{k_0^4}\beta_{23}\cdot\beta_{32})\Big)-$$

$$-\left(\beta_{21}k_z^2 + \beta_{23}k_xk_z\right)\cdot\left(\beta_{12}k_z^2 - \beta_{32}k_xk_z\right)=0 \tag{5}$$

196 Thus, generally Eq. (5) determined the wave numbers for the outgoing waves is of the fourth order (Wait 1996). The

197 boundary conditions at the upper boundary $z = L_{max}$ within the ionosphere F-layer are the absence of the ingoing waves, i.e.

198 the outgoing radiated (leakage) waves are present only. Two roots should be selected that possess the negative imaginary

199 parts $Im(k_{z1, z2}) < 0$, i.e. the outgoing waves dissipate upwards. However, in the case of VLF waves, some simplification can

200 be used. Namely, the expressions for the wave numbers $k_{1,2}$ are obtained from Eqs. (3), where the dependence on x is

201 neglected: $|k_{1,2}| >> k_0$. This approximation is valid within F-layer where the first outgoing wave corresponds to the whistlers

202 with small dissipation, the second one is the highly dissipating slow wave. To formulate the boundary conditions for Eqs.

203 (3a, b) at $z \geq L_{max}$, the EM field components can be presented as:

$$H_x = A_1 e^{-ik_{z1}\tilde{z}} + \alpha_2 A_2 e^{-ik_{z2}\tilde{z}}, \quad H_y = \alpha_1 A_1 e^{-ik_{z1}\tilde{z}} + A_2 e^{-ik_{z2}\tilde{z}} \tag{6}$$

205 In the relations (6) $\tilde{z} = z - L_z$. Eqs. (3) are simplified in the approximation described above:

206

$$\beta_{22}\frac{\partial^2 H_x}{\partial z^2} - \beta_{21}\frac{\partial^2 H_y}{\partial z^2} + k_0^2 H_x = 0, \quad \beta_{11}\frac{\partial^2 H_y}{\partial z^2} - \beta_{12}\frac{\partial^2 H_x}{\partial z^2} + k_0^2 H_y = 0 \tag{7}$$

208

209 The solution of Eqs. (7) is searched for as: $H_{x,y} \sim \exp(-ik_z\tilde{z})$. The following equation has been obtained to get the wave

210 numbers $k_{z1, z2}$ from Eqs. (7):

$$\kappa^4 - (\beta_{22} + \beta_{11})\kappa^2 + \beta_{11}\beta_{22} - \beta_{12}\beta_{21} = 0, \quad \kappa^2 = \frac{k_0^2}{k_z^2} \tag{8}$$

212 Therefore, from Eq. (8) follows,

$$\kappa_{1,2}^2 = \frac{\beta_{11}+\beta_{22}}{2} \pm \left((\frac{\beta_{11}-\beta_{22}}{2})^2 + \beta_{12}\beta_{21}\right)^{1/2}; \alpha_1 = \frac{\beta_{22}-\kappa_1^2}{\beta_{21}} = \frac{\beta_{12}}{\beta_{11}-\kappa_1^2}; \alpha_2 = \frac{\beta_{11}-\kappa_2^2}{\beta_{12}} = \frac{\beta_{21}}{\beta_{22}-\kappa_2^2}; k_{z1,z2}^2 = \frac{k_0^2}{\kappa_{1,2}^2} \tag{9}$$

214

215 The signs of $k_{z1, z2}$ have been chosen from the condition $Im(k_{z1, z2}) < 0$. From Eq. (5) at the upper boundary $z = L_{max}$, the

216 following relations are valid:

$$H_x = A_1 + \alpha_2 A_2, \quad H_y = \alpha_1 A_1 + A_2 \tag{10}$$

218

219 From Eq. (10) one can get

$$220 \qquad A_1 = \Delta^{-1}(H_x - \alpha_2 H_y); A_2 = \Delta^{-1}(H_y - \alpha_1 H_x); \Delta = 1 - \alpha_1\alpha_2 \qquad (11)$$

221   Thus, it is possible to exclude the amplitudes of the outgoing waves $A_{1,2}$ from Eqs. (9). As a result, at $z = L_{max}$ the boundary

222   conditions are rewritten in terms of H_x, H_y only:

$$\frac{\partial H_x}{\partial z} = -i(k_{z1}A_1 + k_{z2}\alpha_2 A_2) = -\frac{i}{\Delta}\left((k_{1z} - \alpha_1\alpha_2 k_{z2})H_x + \alpha_2(k_{z2} - k_{z1})H_y\right)$$

$$\frac{\partial H_y}{\partial z} = -i(k_{z1}\alpha_1 A_1 + k_{z2}A_2) = -\frac{i}{\Delta}\left((k_{z2} - \alpha_1\alpha_2 k_{z1})H_y + \alpha_1(k_{z1} - k_{z2})H_x\right)$$

223   (12)

224   The relations (12) are the upper boundary conditions of the radiation for the boundary $z=L_{max}\sim 250 - 400$ km. These

225   conditions will be transformed/recalculated using the analytical numerical recurrent procedure into equivalent impedance

226   boundary conditions at $z = L_z \sim 70 - 90$ km.

227   Note that in the "whistler/VLF approximation" is valid at frequencies ~ 10 kHz for the F-region of the ionosphere.

228   In this approximation and $k_x \approx 0$, we receive the dispersion equation using Eqs. (5), (8), (9), in the form:

$$229 \qquad k_z'^2 k^2 = k_0^2 g^2 \qquad (13)$$

230   where $k^2 = k_x^2 + k_z^2 = k_x'^2 + k_z'^2$; k_x' and k_z' are the transverse and longitudinal components of wave number relative to

231   geomagnetic field. For F-region of the ionosphere, where $\nu_e \ll \omega \ll \omega_{He}$, Eq. (13) reduces to the standard form of the

232   whistler dispersion equation $|k_z'| k = k_0 |g|$; $g \approx -\omega_{pe}^2/(\omega\omega_{He})$; $\omega = c^2 k |k_z'|(\omega_{He}/\omega_{pe}^2)$. In a special case of the waves

233   propagating along geomagnetic field, $k_x = 0$, for the propagating whistler waves, well-known dispersion dependence is

234    $\omega = c^2 k_z'^2 (\omega_{He}/\omega_{pe}^2)$ (Artcimovich and Sagdeev, 1979). For the formulated problem we can reasonably assume $k_x \approx 0$.

235   Therefore eq. (13) is reduced to $k_z^4 \cos^2\theta = k_0^4 g^2$. As a result, we get $k_{z1} = \sqrt{g/\cos\theta}\,k_0$, $k_{z2} = -i\sqrt{g/\cos\theta}\,k_0$, and then,

236   similarly to the relations (12), the boundary conditions can be presented, in terms of the tangential components of electric

237   field as:

$$238 \qquad \frac{\partial \vec{U}}{\partial z} + \hat{B}\vec{U} = 0 ; \vec{U} = \begin{bmatrix} E_x \\ E_y \end{bmatrix} ; \hat{B} = \frac{1}{2}\sqrt{\frac{g}{\cos\theta}}k_0 \begin{bmatrix} 1+i & -1-i \\ 1+i & 1+i \end{bmatrix} \qquad (14)$$

239

240   Conditions (12) or (14) are the conditions of radiation (absence of ingoing waves) formulated at the upper boundary $z=L_{max}$

241   and suitable for the determination of the energy of the wave leaking from the WGEI into the upper

242   ionosphere/magnetosphere. Note, the equations (12), (14) expressed the boundary conditions of the radiation (more

243   accurately speaking, an absence of incoming waves, what is the consequence to the causality principle), are obtained as a

244   result of limitation by the small parameter $k_x/k_0 |k_x/k_z| \to 0$ in Eq. (5). In spite of the disappearance of the dependence of

245   these boundary conditions explicitly on k_x, the dependence of the characteristics of the wave propagation process on k_x, as a

246   whole, is accounted for, and all results are still valid for the description of the wave beam propagation in the WGEI along the

247   horizontal axis x with finite $k_x \sim k_0$.

3.3 Equivalent Tensor Impedance Boundary Conditions

The tensor impedance at the upper boundary of the effective WGEI $z=L_z$ (see Fig. 1), is obtained by the conditions of radiation (12) or (14), recalculated from the level $z = L_z \sim 80 - 90$ km, placed in the F region of the ionosphere, at $z=L_{max} \sim 250 - 400$ km.

The main idea of the effective tensor impedance method is the unification of analytical and numerical approaches and derivation of the proper impedance boundary conditions without "thin cover layer" approximation. This approximation is usually used in the effective impedance approaches, applied either for artificial or natural layered gyrotropic structures, (see e.g. Tretyakov, 2003; Senior and Volakis, 1995; Kurushin and Nefedov, 1983; Alperovich and Fedorov, 2007). There is one known exception, namely invariant imbedding impedance method (Shalashov and Gospodchikov, 2011; Kim and Kim, 2016). The comparison of our method with the invariant imbedding impedance method will be presented at the end of this subsection. Eqs. (3) jointly with the boundary conditions (12), have been solved by finite differences. The derivatives in Eqs. (3) are approximated as

$$\frac{\partial}{\partial z}\left(C(z)\frac{\partial H_x}{\partial z}\right) \approx \frac{1}{h}\left(C(z_{j+1/2})\frac{(H_x)_{j+1}-(H_x)_j}{h} - C(z_{j-1/2})\frac{(H_x)_j-(H_x)_{j-1}}{h}\right),$$

$$\frac{\partial}{\partial z}\left(F(z)H_x\right) \approx \frac{1}{2h}\left(F(z_{j+1})(H_x)_{j+1} - F(z_{j-1})(H_x)_{j-1}\right) \quad \text{etc.} \tag{15}$$

In Eq. (15) $z_{j+1/2} = h \cdot (j+0.5)$. In Eqs. (10) the approximation is $\partial H_x / \partial z \approx [(H_x)_N - (H_x)_{N-1}]/h$. Here h is the discretization step along OZ axis; N is the total number of nodes. At each step j the difference approximations of Eqs. (3) take the form:

$$\hat{\alpha}_j^{(-)} \cdot \vec{H}_{j-1} + \hat{\alpha}_j^{(0)} \cdot \vec{H}_j + \hat{\alpha}_j^{(+)} \cdot \vec{H}_{j+1} = 0 \tag{16}$$

where $\vec{H}_j = \begin{pmatrix} H_x \\ H_y \end{pmatrix}$, $j = N-1, N-2, ..., 1$, $z_j = h \cdot j$, $L_z = h \cdot N$. Due to the complexity of expressions for the matrix coefficients in Eq. (16) we have shown them in Appendix. The set of the matrix Eq. (16) has been solved by factorization method also known as an elimination/matrix sweep method (see Samarskii, 2001). It can be written as:

$$\vec{H}_j = \hat{b}_j \cdot \vec{H}_{j-1}, \quad j = N, ..., 1 \tag{17a}$$

$$H_{xj+1} = b_{11j+1}H_1 + b_{12j+1}H_2; \; H_{yj+1} = b_{21j+1}H_1 + b_{22j+1}H_2; \; H_1 \equiv H_{xj}; \; H_2 \equiv H_{yj} \tag{17b}$$

This method is a variant of the Gauss elimination method for the matrix 3-diagonal set of the Eq. (16). The value of $\hat{b}_N$ is obtained from the boundary conditions (12) as:

$$\hat{\alpha}_N^{(-)} \cdot \vec{H}_{N-1} + \hat{\alpha}_N^{(0)} \cdot \vec{H}_N = 0 \tag{18}$$

10

274 Therefore $\hat{b}_N = -(\hat{\alpha}_N^{(0)})^{-1} \cdot \hat{\alpha}_N^{(-)}$. Then the matrices $\hat{b}_j$ have been computed sequentially down to the desired value of z =

275 $L_z = h \cdot N_z$, where the impedance boundary conditions are assumed to be applied. At each step the expression for $\hat{b}_j$ follow

276 from (16), (17) as:

$$(\hat{\alpha}_j^{(0)} + \hat{\alpha}_j^{(+)} \cdot \hat{b}_{j+1}) \cdot \vec{H}_j = -\hat{\alpha}_j^{(-)} \cdot \vec{H}_{j-1} \tag{19}$$

278 Therefore, for (17), we obtain $\hat{b}_j = -(\hat{\alpha}_j^{(0)} + \hat{\alpha}_j^{(+)} \cdot \hat{b}_{j+1})^{-1} \cdot \hat{\alpha}_j^{(-)}$. The derivatives in Eqs. (4) have been approximated as:

$$279 \quad (\frac{\partial H_x}{\partial z})_{N_z} \approx \frac{(H_x)_{N_z+1} - (H_x)_{N_z}}{h} = \frac{(b_{N_z+1 \ \ 11} - 1) \cdot (H_x)_{N_z} + b_{N_z+1 \ \ 12} \cdot (H_y)_{N_z}}{h} \tag{20}$$

280 and similar equation can be obtained for $(\frac{\partial H_y}{\partial z})_{N_z}$. Note, that as a result of this discretization, only the values at the grid

281 level N_z are included into the numerical approximation of the derivatives $\partial H_{x,y} / \partial z$ at $z = L_z$. We determine tensor

282 impedance $\hat{Z}$ at $z=L_z \sim 85$ km level. The tensor values are included into the following relations, all of which are

283 corresponded to altitude (in other words, to the grid with number N_z, corresponded to this altitude):

$$284 \quad \vec{n} \times \vec{E} = \hat{Z}_0 \cdot \vec{H}, \ \vec{n} = (0,0,1) \ \text{or} \ E_x = Z_{021} H_x + Z_{022} H_y; \ E_y = -Z_{011} H_x - Z_{012} H_y \tag{21}$$

285 The equivalent tensor impedance is obtained using a two-step procedure. (1) We obtain the matrix $\hat{b}_j$ using Eqs. (3a, b) with

286 the boundary conditions (12) and the procedure (17) – (19) described above. (2) Placing the expressions (21) with tensor

287 impedance into the left parts and the derivatives $\partial H_{x,y} / \partial z$ in the form (20) into the right parts of Eqs. (4), the analytical

288 expressions for the components of the tensor impedance are:

289 $$Z_{011} = -\frac{i}{k_0 h} \left(\frac{\beta_{21}}{1 - \beta_{22} \frac{k_x^2}{k_0^2}} \cdot b_{21} - \frac{\beta_{22}}{1 - \beta_{22} \frac{k_x^2}{k_0^2}} \cdot (b_{11} - 1) \right),$$

290 $$Z_{012} = -\frac{i}{k_0 h} \left(\frac{\beta_{21}}{1 - \beta_{22} \frac{k_x^2}{k_0^2}} \frac{\partial H_y}{\partial z} \cdot (b_{22} - 1) - \frac{\beta_{22}}{1 - \beta_{22} \frac{k_x^2}{k_0^2}} \cdot b_{12} - k_x h \cdot \frac{\beta_{23}}{1 - \beta_{22} \frac{k_x^2}{k_0^2}} \right),$$

291 $$Z_{021} = \frac{i}{k_0 h} \left((\beta_{11} + \frac{k_x^2}{k_0^2} \frac{\beta_{12} \cdot \beta_{21}}{1 - \beta_{22} \frac{k_x^2}{k_0^2}}) \cdot b_{21} - \frac{\beta_{12}}{1 - \beta_{22} \frac{k_x^2}{k_0^2}} \cdot (b_{11} - 1) \right),$$

11

292
$$Z_{022} = \frac{i}{k_0 h}\left((\beta_{11} + \frac{k_x^2}{k_0^2}\frac{\beta_{12}\cdot\beta_{21}}{1 - \beta_{22}\frac{k_x^2}{k_0^2}})\cdot(b_{22} - 1) - k_x h\cdot(\beta_{13} + \frac{k_x^2}{k_0^2}\frac{\beta_{12}\cdot\beta_{23}}{1 - \beta_{22}\frac{k_x^2}{k_0^2}}) - \frac{\beta_{12}}{1 - \beta_{22}\frac{k_x^2}{k_0^2}}\cdot b_{12} \right)$$ (22)

293

294   The proposed method of the transfer of the boundary conditions from the ionosphere F-layer $L_{max} = 250 - 400$ km into the

295   lower part of the E-layer $L_z = 80 - 90$ km is stable and easily realizable in comparison with some alternative approaches

296   based on the invariant imbedding methods (Shalashov and Gospodchikov, 2011; Kim and Kim, 2016). The stability of our

297   method is due to the stability of the Gauss elimination method when the coefficients at the matrix central diagonal are

298   dominating. The last is valid for the ionosphere with electromagnetic losses where the absolute values of the permittivity

299   tensor are large. The application of the proposed matrix sweep method in the media without losses may require the use of the

300   Gauss method with the choice of the maximum element, to ensure the stability. However, as our simulations (not presented

301   here) demonstrated, for the electromagnetic problems in the frequency domain, the simple Gauss elimination and the choice

302   of the maximal element give the same results. The accumulation of errors may occur in evolutionary problems in the time

303   domain, when the Gauss method should be applied sequentially many times. The use of the independent functions H_x, H_y in

304   Eqs. (3) seems natural, as well as the transfer (17a), because the impedance conditions are the expressions of the electric E_x,

305   E_y through these magnetic components H_x, H_y at the upper boundary of the VLF waveguide $80 - 90$ km. The naturally

306   chosen direction of the recalculation of the upper boundary conditions from $z = L_{max}$ to $z = L_z$, i.e. from upper layer with

307   large impedance value to lower altitude layer with relatively small impedance value, provides, at the same time, the stability

308   of the simulation procedure. The obtained components of the tensor impedance $\hat{Z}_0$ are small, $|Z_{0\alpha\beta}| \leq 0.1$. This determines

309   the choice of the upper boundary $z = L_z$ for the effective WGEI. Due to small impedance, EM waves incident from below on

310   this boundary are reflected effectively back. Therefore, the region $0 \leq z \leq L_z$ indeed can be presented as an effective WGEI.

311   This waveguide includes not only lower boundary at $L_{ISO} \sim 65 - 75$ km with rather small losses, but also thin dissipative and

312   anisotropic/gyrotropic layer between 75 and $85 - 90$ km.

313   Finally, the main differences and advantages of the proposed tensor impedance method from other methods for

314   impedance recalculating and in particular invariant imbedding methods (Shalashov and Gospodchikov, 2011; Kim and Kim,

315   2016) can be summarised as follows:

316   (i) in contrast to invariant imbedding method currently proposed method can be used for direct recalculation of

317   tensor impedance as it determined analytically, see Eqs. (22).

318   (ii) for the media without non-locality, proposed method does not require to solve integral equation(s).

319   (iii) the proposed method does not require forward and reflected waves. The conditions for the radiation at the upper

320   boundary $z = L_{max}$ (see Eqs. (12)) are determined through the total field components $H_{x,y}$, which simplify the overall

321   calculations.

322   (iv) the overall calculation procedure is very effective and computationally stable. Note, that even for the very low-

323   loss systems, the required level of stability can be achieved with modification based on the choice of the maximal element

324   for matrix inversion.

3.4 Propagation of Electromagnetic Waves in the Gyrotropic Waveguide and the TIMEB Method

327   Let's use the transverse components of electric E_y, and magnetic H_y fields to derive equations for the slow varying

328   amplitudes $A(x,y,z)$, $B(x,y,z)$ of the VLF beams. These components can be represented as:

$$E_y = \frac{1}{2} A(x,y,z) \cdot e^{i\omega t - ik_0 x} + c.c., \quad H_y = \frac{1}{2} B(x,y,z) \cdot e^{i\omega t - ik_0 x} + c.c. \tag{23}$$

330   Here we assumed $k_x = k_0$ to reflect beam propagation in the WGEI with the main part in the atmosphere and lower

331   ionosphere (*D*-region) which are similar to free space by its electromagnetic parameters. The presence of a thin anisotropic

332   and dissipative layer belonging to the *E*-region (Guglielmi and Pokhotelov, 1996) of the ionosphere causes, altogether with

333   the impedance boundary condition, the proper z dependence of $B(x,y,z)$. Using (21) and (22), the boundary conditions are

334   determined at the height $z = L_z$ for the slowly varying amplitudes $A(x,y,z)$, $B(x,y,z)$ of the transverse components E_y, H_y. As it

335   follows from Maxwell's equations, the components E_x and H_x through E_y, H_y in the method of beams have the form:

$$H_x \approx -\frac{i}{k_0} \frac{\partial E_y}{\partial z}, \quad E_x \approx \gamma_{12} E_y + i \frac{\tilde{\beta}_{33}}{k_0} \frac{\partial H_y}{\partial z} + \tilde{\beta}_{13} H_y \tag{24}$$

337   where $\gamma_{12} = \Delta_0^{-1}(\varepsilon_{13}\varepsilon_{32} - \varepsilon_{12}\varepsilon_{33}), \ \tilde{\beta}_{13} = \Delta_0^{-1}\varepsilon_{13}, \ \tilde{\beta}_{33} = \Delta_0^{-1}\varepsilon_{33}; \ \Delta_0 = \varepsilon_{11}\varepsilon_{33} - \varepsilon_{13}\varepsilon_{31}.$ From Eqs. (21) and (24), the boundary

338   conditions for *A*, *B* can be defined as:

$$A - \frac{i}{k_0} Z_{11} \cdot \frac{\partial A}{\partial z} + Z_{12} \cdot B \approx 0, \quad \gamma_{12} \cdot A + \frac{i}{k_0} Z_{21} \cdot \frac{\partial A}{\partial z} + (\tilde{\beta}_{13} - Z_{22}) \cdot B + \frac{i}{k_0} \tilde{\beta}_{33} \cdot \frac{\partial B}{\partial z} \approx 0 \tag{25}$$

341   The evolution equations for the slowly varying amplitudes $A(x,y,z)$, $B(x,y,z)$ of the VLF beams are derived. The

342   monochromatic beams are considered, when the frequency ω is fixed and the amplitudes do not depend on time *t*. Looking

343   for the solutions for the EM field as $\vec{E}, \vec{H} \sim \exp(i\omega t - ik_x x - ik_y y).$, Maxwell's equations are:

$$-ik_y H_z - \frac{\partial H_y}{\partial z} = ik_0 D_x, \quad \frac{\partial H_x}{\partial z} + ik_x H_z = ik_0 D_y, \quad -ik_x H_y + ik_y H_x = ik_0 D_z$$

$$-ik_y E_z - \frac{\partial E_y}{\partial z} = -ik_0 H_x, \quad \frac{\partial E_x}{\partial z} + ik_x E_z = -ik_0 H_y, \quad -ik_x E_y + ik_y E_x = -ik_0 H_z \tag{26}$$

345   Here $D_x = \varepsilon_{11} E_x + \varepsilon_{12} E_y + \varepsilon_{13} E_z$. From Eqs. (21), the equations for E_x, E_z through E_y, H_y are:

13

346

$$E_x = \frac{1}{\Delta_y}\left\{[\varepsilon_{13}\cdot\varepsilon_{32} - (\varepsilon_{12} + \frac{k_x k_y}{k_0^2})\cdot(\varepsilon_{33} - \frac{k_y^2}{k_0^2})]E_y + \frac{i}{k_0}(\varepsilon_{33} - \frac{k_y^2}{k_0^2})\frac{\partial H_y}{\partial z} + \frac{k_x}{k_0}\varepsilon_{13}\cdot H_y + \frac{ik_y}{k_0^2}\varepsilon_{13}\frac{\partial E_y}{\partial z}\right\}$$

$$E_z = \frac{1}{\Delta_y}\left\{[\varepsilon_{31}\cdot(\varepsilon_{12} + \frac{k_x k_y}{k_0^2}) - \varepsilon_{32}\cdot(\varepsilon_{11} - \frac{k_y^2}{k_0^2})]E_y - \frac{i}{k_0}\varepsilon_{31}\frac{\partial H_y}{\partial z} - \frac{k_x}{k_0}\cdot(\varepsilon_{11} - \frac{k_y^2}{k_0^2})H_y - \frac{ik_y}{k_0^2}\cdot(\varepsilon_{11} - \frac{k_y^2}{k_0^2})\frac{\partial E_y}{\partial z}\right\}$$

(27)

347   In Eq. (27), $\Delta_y \equiv (\varepsilon_{11} - \frac{k_y^2}{k_0^2})\cdot(\varepsilon_{33} - \frac{k_y^2}{k_0^2}) - \varepsilon_{31}\cdot\varepsilon_{13}$. The equations for E_y, H_y obtained from the Maxwell equations are:

348

$$\left(\frac{\partial^2}{\partial z^2} - k_x^2 - k_y^2\right)E_y + ik_y\left(\frac{\partial E_z}{\partial z} - ik_x E_x - ik_y E_y\right) + k_0^2 D_y = 0; \quad -ik_0\frac{\partial E_x}{\partial z} + k_x k_0 E_z + k_0^2 H_y = 0$$

(28)

349   After substitution of (27) for E_x, E_z into Eqs. (28), the coupled equations for E_y, H_y can be derived. The follow expansion
350   should be used: $k_x = k_0 + \delta k_x$, $|\delta k_x| \ll k_0$, also $|k_y| \ll k_0$. Then, according to (Weiland and Wilhelmsson, 1977):

351

$$-i\cdot\delta k_x \to \frac{\partial}{\partial x}, \quad -i\cdot k_y \to \frac{\partial}{\partial y}$$

(29)

352   The expansions should be until the quadratic terms of k_y and the linear terms of δk_x. As a result, parabolic equations (Levy
353   2000) for the slowly varying amplitudes A and B are derived. In the lower ionosphere/atmosphere, where the effective
354   permittivity reduces to a scalar $\varepsilon(\omega,z)$, they are independent:

355

$$\frac{\partial A}{\partial x} + \frac{i}{2k_0}\left(\frac{\partial^2 A}{\partial y^2} + \frac{\partial^2 A}{\partial z^2}\right) + \frac{ik_0}{2}\cdot(\varepsilon - 1)A = 0$$

$$\frac{\partial B}{\partial x} + \frac{i}{2k_0}\left(\frac{1}{\beta}\frac{\partial}{\partial z}(\beta\frac{\partial B}{\partial z}) + \frac{\partial^2 B}{\partial y^2}\right) + \frac{ik_0}{2}\cdot(\varepsilon - 1)B = 0$$

(30a)

356

357   Here $\beta \equiv \varepsilon^{-1}$. Accounting for the presence of gyrotropic layer and the tensor impedance boundary conditions at the upper
358   boundary $z = L_z$ of the VLF waveguide, the equations for the slowly varying amplitudes in the general case are:

359

$$\frac{\partial A}{\partial x} + \frac{i}{2k_0}\left(\frac{\partial^2 A}{\partial y^2} + \frac{\partial^2 A}{\partial z^2}\right) + \frac{ik_0}{2}\cdot(\tilde{\varepsilon}_{22} - 1)\cdot A + \frac{\gamma_{21}}{2}\frac{\partial B}{\partial z} + \frac{ik_0}{2}\cdot\gamma_{23}B = 0$$

$$\frac{\partial B}{\partial x} + \frac{i}{2k_0}\left(\frac{1}{\tilde{\beta}_{11}}\frac{\partial}{\partial z}(\tilde{\beta}_{33}\frac{\partial B}{\partial z}) + \frac{\partial^2 B}{\partial y^2}\right) + \frac{i}{2\tilde{\beta}_{11}}\frac{\partial}{\partial z}(\gamma_{12}A) + \frac{1}{2\tilde{\beta}_{11}}\frac{\partial}{\partial z}(\tilde{\beta}_{13}B) + \frac{ik_0}{2\tilde{\beta}_{11}}\gamma_{32}A + \frac{\tilde{\beta}_{31}}{2\tilde{\beta}_{11}}\frac{\partial B}{\partial z} + \frac{ik_0}{2}\cdot(\frac{1}{\tilde{\beta}_{11}} - 1)\cdot B = 0$$

(30b)

360   In Eqs. (30b),

$$\gamma_{12} \equiv \frac{\varepsilon_{13}\cdot\varepsilon_{32} - \varepsilon_{12}\cdot\varepsilon_{33}}{\Delta}, \gamma_{21} \equiv \frac{\varepsilon_{23}\cdot\varepsilon_{31} - \varepsilon_{21}\cdot\varepsilon_{33}}{\Delta}, \gamma_{23} \equiv \frac{\varepsilon_{21}\cdot\varepsilon_{13} - \varepsilon_{23}\cdot\varepsilon_{11}}{\Delta}, \gamma_{32} \equiv \frac{\varepsilon_{31}\cdot\varepsilon_{12} - \varepsilon_{32}\cdot\varepsilon_{11}}{\Delta}, \tilde{\beta}_{11} \equiv \frac{\varepsilon_{11}}{\Delta}, \tilde{\beta}_{13} \equiv \frac{\varepsilon_{13}}{\Delta},$$

$$\tilde{\beta}_{31} \equiv \frac{\varepsilon_{31}}{\Delta}, \tilde{\beta}_{33} \equiv \frac{\varepsilon_{33}}{\Delta}; \Delta \equiv \varepsilon_{11}\cdot\varepsilon_{33} - \varepsilon_{13}\cdot\varepsilon_{31}; \tilde{\varepsilon}_{22} \equiv \varepsilon_{22} + \frac{\varepsilon_{21}(\varepsilon_{13}\varepsilon_{32} - \varepsilon_{12}\varepsilon_{33}) + \varepsilon_{23}(\varepsilon_{31}\varepsilon_{12} - \varepsilon_{32}\varepsilon_{11})}{\Delta}$$

362   Eqs. (30b) are reduced to Eqs. (30a) when the effective permittivity is scalar. At the Earth's surface $z = 0$, the impedance
363   conditions are reduced, accounting for that the medium is isotropic and the conductivity of the Earth is finite, to the form:

14

364 $$E_y = Z_{0E} H_x, \quad E_x = -Z_{0E} H_y, \quad Z_{0E} \equiv \left(\frac{i\omega}{4\pi\sigma_E} \right)^{1/2} \tag{31a}$$

366 Here $\sigma_E \sim 10^8$ s^{-1} is the Earth's conductivity. The boundary conditions (31a) at the Earth's surface, where

367 $Z_{022} = Z_{021} \equiv Z_{0E}$, $Z_{012} = Z_{021} = 0$, $\beta_{33} = \varepsilon^{-1}(z=0)$, $\gamma_{12} = 0$, $\tilde{B}_{13} = 0$, can be rewritten as

368 $$E_y + \frac{i}{k_0} Z_{0E} \frac{\partial E_y}{\partial z} = 0, \quad \frac{i}{\varepsilon(z=0)k_0} \frac{\partial H_y}{\partial z} + Z_{0E} H_y = 0 \tag{31b}$$

370 Eqs. (30), combined with the boundary conditions (25) at the upper boundary of the VLF waveguide $z = L_z$, and with the
371 boundary conditions at the Earth's surface (31b), are used to simulate the VLF wave propagation. The surface impedance of
372 the Earth has been calculated from the Earth's conductivity, see eq. (31a). The boundary conditions to solution of Eqs. (30),
373 (25), (31b) are chosen in the form

374 $$A(x=0, y, z) = 0, \ B(x=0, y, z) = B_0 \exp\left(-\left((y-0.5L_y)/y_0\right)^{2n}\right)\exp\left(-\left((z-z_1)/z_0\right)^{2n}\right), \ n = 2 \tag{32}$$

375 In relations (32), z_1, z_0, y_0 and B_0 are the vertical position of maximum value, the vertical and transverse characteristic
376 dimensions of the spatial distribution and the maximum value of H_y, respectively at the input of the system, $x = 0$. The
377 size of the computing region along OY axis is, by the order of value, $L_y \sim 2000$ km. Because the gyrotropic layer is relatively
378 thin and is placed at the upper part of the VLF waveguide, the beams are excited near the Earth's surface, the wave
379 diffraction in this gyrotropic layer along OY axis is quite small, i.e. the terms $\partial^2 A/dy^2$, $\partial^2 B/dy^2$ are small there as well.
380 Contrary to this, the wave diffraction is very important in the atmosphere in the lower part of the VLF waveguide, near the
381 Earth's surface. To solve the problem of the beam propagation, the method of splitting with respect to physical factors has
382 been applied (Samarskii 2001). Namely, the problem has been approximated by the finite differences:

383 $$\vec{C} \equiv \begin{pmatrix} A \\ B \end{pmatrix}, \quad \frac{\partial \vec{C}}{\partial x} + \hat{L}_y \vec{C} + \hat{L}_z \vec{C} = 0 \tag{33}$$

384 In the terms $\hat{L}_y \vec{C}$, the derivatives with respect to y are included, whereas all other terms are included into $\hat{L}_z \vec{C}$. Then the
385 following fractional steps have been applied, the first one is along y, the second one is along z:

386 $$\frac{\vec{C}^{p+1/2} - \vec{C}^p}{h_x} + \hat{L}_y \vec{C}^{p+1/2} = 0, \quad \frac{\vec{C}^{p+1} - \vec{C}^{p+1/2}}{h_x} + \hat{L}_z \vec{C}^{p+1} = 0 \tag{34}$$

387 The region of simulation is $0 < x < L_x = (1000 - 2000)$ km, $0 < y < L_y = (2000 - 3000)$ km, $0 < z < L_z = 80 - 90$ km. The
388 numerical scheme (34) is absolutely stable. Here h_x is the step along OX axis, $x_p = p\,h_x$, $p = 0, 1, 2,\ldots$. This step has been
389 chosen from the conditions of the simulation results independence on the diminishing h_x.

15

390
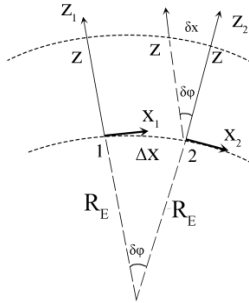
Figure 2. The rotation of the local Cartesian coordinate frame at each step along the Earth's surface h_x on a small angle $\delta\varphi \approx \approx \Delta x/R_E$, radians, while $\Delta x = h_x$. The following strong inequalities are valid $h_x \ll L_z \ll R_E$. At the Earth's surface $z = 0$.

On the simulation at each step along *OX* axis, the correction on the Earth's curvature has been inserted in adiabatic manner applying the rotation of the local coordinate frame *XOZ*. Because the step along *x* is small $h_x \sim 1$ km $\ll L_z$, this correction of the $\vec{C}$ results in the multiplier *exp(-ik₀·δx)*, where *δx = z·(hₓ/R_E)*, $R_E \gg L_z$ is the Earth's radius (see Fig. 2 and the caption to this figure). At the distances $x \leq 1000$ km, the simulation results do not depend on the insertion of this correction, whereas at higher distances some quantitative difference occurs: the VLF beam propagates more closely to the upper boundary of the waveguide.

3.5 VLF Waveguide Modes and Reflection from the VLF Waveguide Upper Effective Boundary

In general, our model needs the consideration of the waveguide modes excitations by a current source such as dipole-like VLF radio source and lightning discharge. Then, the reflection of the waves incident on the upper boundary ($z=L_z$) of the effective WGEI can be considered. There will be possible to demonstrate that this structure has indeed good enough waveguiding properties. Then, in the model described in the present paper, the VLF beam is postulated already on the input of the system. To understand, how such a beam is excited by the, say, dipole antenna near the lower boundary $z=0$ of the WGEI, the formation of the beam structure based on the mode presentation should be searched. Then the conditions of the radiation (absence of ingoing waves) (12) can be used as the boundary conditions for the VLF beam radiated to the upper ionosphere/magnetosphere. Due to a relatively large scale of the inhomogeneity in this region, the complex geometrical optics (Rapoport et al., 2014) would be quite suitable for modeling a beam propagation, even accounting for the wave dispersion in magnetized plasma. The proper effective boundary condition, similarly to (Rapoport et al., 2014) would allow to make relatively accurate matching between the regions, described by the full wave electromagnetic approach with Maxwell's equations and complex geometrical optics (FWEM-CGO approach). All of these materials are not included in this paper, but will be delivered in the two future papers. The first paper will be dedicated to the modeling VLF waves propagating in WGEI based on the field expansion as a set of eigenmodes of the waveguide (the mode presentation

16

approach). The second paper will deal with the leakage of the VLF beam from the WGEI into the upper ionosphere and

417   magnetosphere and the VLF beam propagation in these media. Here we describe only one result, which concerns the mode

418   excitation in the WGEI, because this result is principally important for the justification of TIMEB method. It was shown that

419   more than five lowest modes of the WGEI are strongly localized in the atmosphere-lower ionosphere. Their longitudinal

420   wavenumbers are close to the corresponding wavenumbers of EM-waves in the atmosphere. This fact convinced that the

421   TIMEB method can be applied to the propagation of the VLF electromagnetic waves in the WGEI.

4. Modeling Results

423   The dependencies of the permittivity components ε_1, ε_3, ε_h in the coordinate frame associated with the geomagnetic field $\vec{H}_0$

424   are given in Fig. 3. The parameters of the ionosphere used for modeling are taken from (Al'pert 1972; Alperovich and

425   Fedorov 2007; Kelley 2005; Schunk and Nagy 2010; Jursa 1985). The typical results of simulations are presented in Fig. 4.

426   The parameters of the ionosphere correspond to Fig. 3. The angle θ (Fig. 1) is 45°. The VLF frequency is $\omega = 10^5$ s^{-1}, $f =$

427      $\omega/2\pi \approx 15.9$ kHz. The Earth's surface is assumed as ideally conductive at the level $z = 0$. The values of EM-field are given in

428   absolute units. The magnetic field is measured in Oersteds (Oe), or Gauss (Gs), 1 Gs = 10^{-4} T, whereas the electric field is

429   also in Gs, 1 Gs = 300 V/cm.

430   Note that in the absolute (Gaussian) units the magnitudes of the magnetic field component $|H_y|$ are the same as ones of the

431   electric field component $|E_z|$ in the atmosphere region where the permittivity is $\varepsilon \approx 1$. Below in the Fig. 4 caption, the

432   correspondence between the absolute units and practical SI units is given.

433   It is seen that the absolute values of the permittivity components increase sharply above $z = 75$ km. The behavior of

434   the permittivity components is step-like, as seen from Fig. 3a. Therefore, the results of simulations are tolerant to the choice

435   of the upper wall position of the Earth's surface–ionosphere waveguide. The computed components of the tensor impedance

436   at $z = 85$ km are: $Z_{011} = 0.087 + i0.097$, $Z_{021} = 0.085 + i0.063$, $Z_{012} = -0.083 - i0.094$, $Z_{022} = 0.093 + i0.098$. So, a condition

437      $|Z_{0\alpha\beta}| \leq 0.15$ is satisfied there, which is necessary for the applicability of the boundary conditions (25). The maximum value

438   of the H_y component is 0.1 Oe = 10^{-5} T in Fig. 4a for the initial VLF beam at $x = 0$. This corresponds to the value of E_z

439   component of 0.1 Gs = 30 V/cm. At the distance $x = 1000$ km the magnitudes of the magnetic field H_y are of about 3$^\cdot$ 10^{-5}

440   Oe = 3 nT, whereas the electric field E_y is of 3$^\cdot$ 10^{-6} Gs ≈ 1 mV/cm.

441   **a**   **b**   **c**   **d**

442

e   f   g
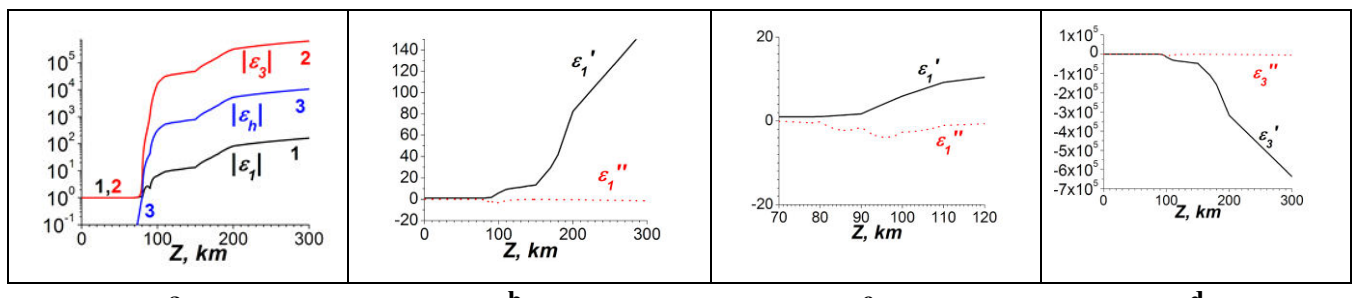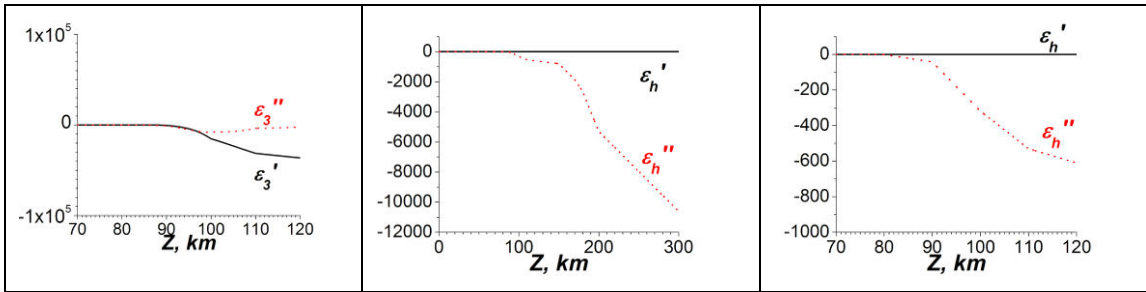
Figure 3. (a) The vertical dependencies of the modules of components of the permittivity in the frame associated with the geomagnetic field $|\varepsilon_l|$, $|\varepsilon_3|$, $|\varepsilon_h|$,, curves 1, 2, 3 correspondingly. (b) – (g) The real (corresponding lines with the values denoted by one prime) and imaginary (corresponding lines with the values denoted by two primes) parts of the components ε_l, ε_3, ε_h, general and detailed views.

447

448   a   b   c

449

450   d   e
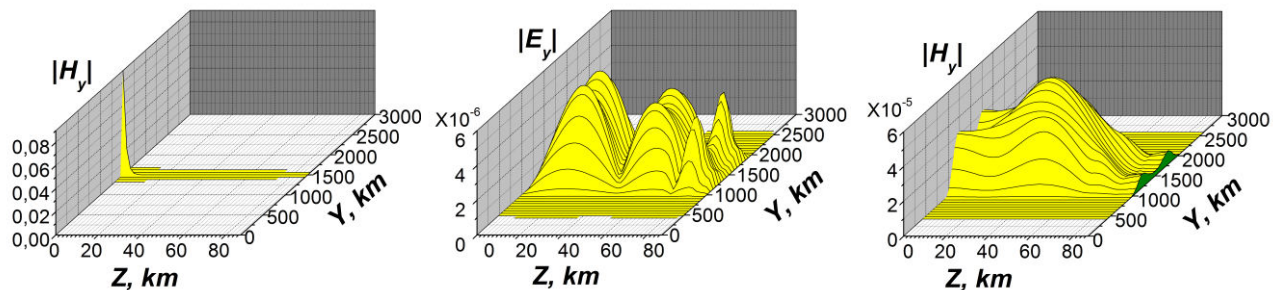
Figure 4. Part a) is the initial distribution of $|H_y|$ at $x = 0$. Parts b), c) are $|E_y|$ and $|H_y|$ at $x = 600$ km. Parts d), e) are $|E_y|$ and $|H_y|$ at $x = 1000$ km. For the electric field maximum value (Fig. d) is $3 \cdot 10^{-6}$ Gs ≈ 1 mV/cm, for the magnetic field maximum value (Fig. e) is $3 \cdot 10^{-5}$ Gs ≈ 3 nT. At the altitudes $z < 75$ km, $|E_z| \approx |H_y|$. $\omega = 1 \cdot 10^5 \, s^{-1}$; $\theta = 45°$

The wave beams are localized within the WGEI, $0 < z < 75$ km, mainly in the regions with the isotropic permittivity (see Fig. 4b-e). The mutual transformations of the beams of different polarizations occur near the waveguide upper boundary due to the anisotropy of the ionosphere within the thin layer 75 km $< z <$ 85 km (Fig. 4b, d). These transformations depend on the permittivity component values of the ionosphere at the altitude $z > 80$ km and on the components of the tensor

18

458   impedance. Therefore, the measurements of the phase and amplitude modulations of different EM components near the

459   Earth's surface can provide information on the properties of the lower and middle ionosphere.

460   In accordance with boundary condition (32), we suppose that when entering the system (at $X = 0$), only one of the two

461   polarization modes is excited, namely, the TM mode, i.e. at $X = 0$, $H_y \neq 0$; $E_y = 0$ (Fig. 4a). Upon further propagation of the

462   beam with such boundary conditions at the entrance to the system in a homogeneous isotropic waveguide, the property of the

463   electromagnetic field described by the relation $H_y \neq 0$; $E_y = 0$ will remain valid. The qualitative effect due to the presence

464   of gyrotropy (a) in a thin bulk layer near the upper boundary of WGEI and (b) in the upper boundary condition with complex

465   gyrotropic and anisotropic impedance is as follows. During beam propagation in the WGEI, the TE polarization mode with

466   the corresponding field components, including E_y, is also excited. This effect is illustrated in Figs. 4 b, d.

467   The magnitude of the E_y component depends on the values of the electron concentration at the altitudes $z = 75 - 100$ km. In

468   Fig. 5a, b the different dependencies of the electron concentration $n(z)$ are shown (see solid (1), dash (2) and dot (3) lines).

469   The corresponding dependencies of the component absolute values of the permittivity are shown in Figs. 4c and 4d.

470   **a**   **b**   **c**   **d**
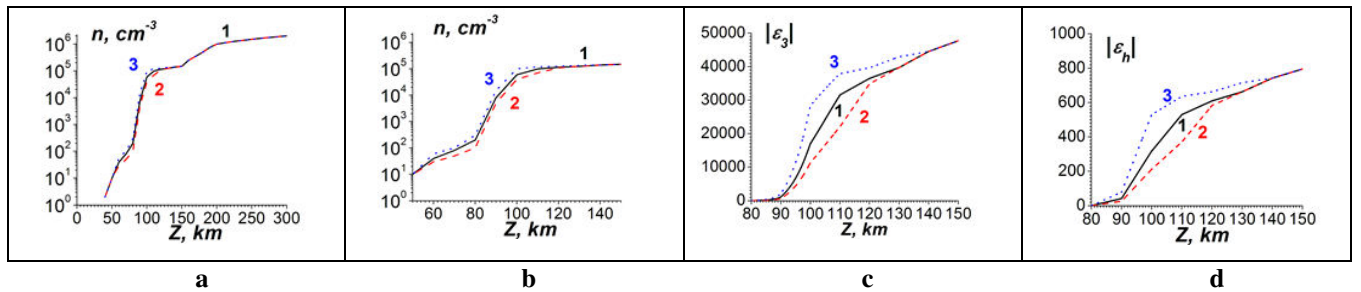
471 **Figure 5. Different profiles of the electron concentration *n(z)* used in simulations: solid, dash, and dot lines correspond to**
472 **undisturbed, decreased and increased concentrations, respectively. (a) the detailed view; (b) general view; (c) and (d) the**
473 **permittivity $|\varepsilon_3|$ and $|\varepsilon_h|$ modules.**

474

475   The distributions of $|E_y|$, $|H_y|$ at $x = 1000$ km are given in Fig. 6. Results in Figs. 6a and 6b correspond to the solid (1) curve

476     $n(z)$ in Fig. 5; Figs. 6c and 6d correspond to the dash (2) curve; Figs. 6e and 6f correspond to the dot (3) curve in Fig. 5. The

477   initial H_y beam is the same and is given in Fig. 4a. The values of the tensor impedance for these three cases are presented in

478   Table 1.

479

480 **Table 1. The values of tensor impedance components corresponded to the data shown in Fig. 5.**

Component of the tensor impedance	Z_{011}	Z_{021}	Z_{012}	Z_{022}
Undisturbed concentration (curves 1 in Fig. 5)	0.088 + i0.098	0.085 + i0.063	−0.083 – i0.094	0.093 + i0.098
Decreased concentration	0.114 + i0.127	0.107 + i0.079	−0.105 – i0.127	0.125 + i0.125

(curves 2 in Fig. 5)				
Increased concentration (curves 3 in Fig. 5)	$0.067 + i0.0715$	$0.061 + i0.051$	$-0.060 - i0.070$	$0.069 + i0.072$

481

482

483
        a   b   c


484

485
        d   e   f
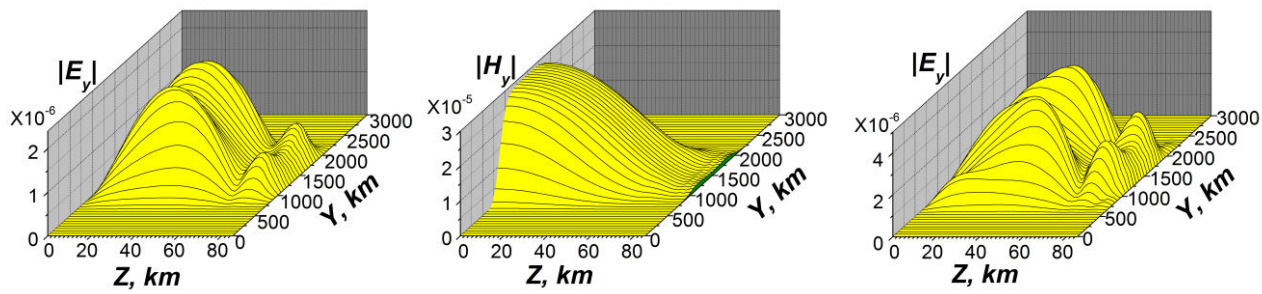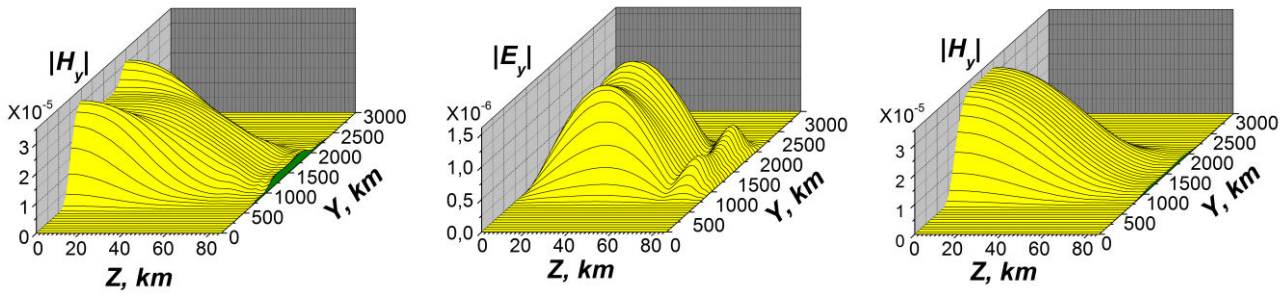
486 **Figure 6. Parts a), c), e) are dependencies of $|E_y|$, parts b), d), f) are dependencies of $|H_y|$ at $x = 1000$ km; $\omega = 1 \cdot 10^5 s^{-1}$; $\theta = 45°$.**
487 **The initial beams are the same as in Fig. 4, a). Parts a), b) correspond to the solid (1) curves in Fig. 5; parts c), d) are for the dash**
488 **(2) curves; parts e), f) correspond to the dot (3) curves there.**
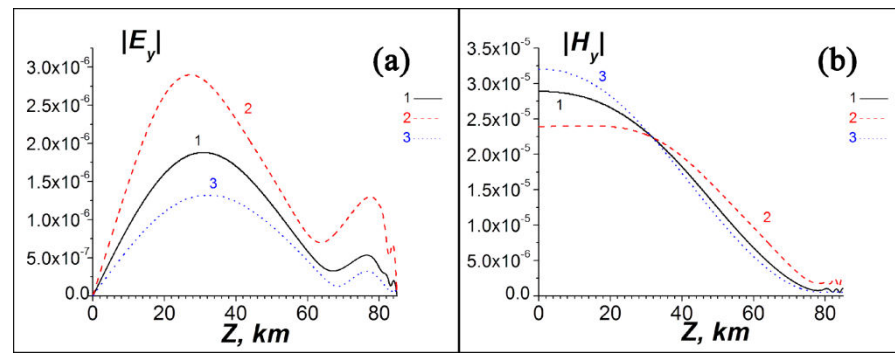
489

490 **Figure 7. The dependencies of EM components on the altitude z in the center of the waveguide, $y = 1500$ km, for the different**
491 **profiles of the electron concentration. The solid (1), dash (2), and dot (3) curves correspond to the different profiles of the electron**
492 **concentration in Fig. 5, a), b), the same kinds of curves; $\omega = 1 \cdot 10^5 s^{-1}$; $\theta = 45°$**

493 The distributions of $|E_y|$, $|H_y|$ on z at x = 1000 km in the center of the waveguide, y = 1500 km, are given in Fig. 7. These
494 simulations show that the change in the complex tensors of both volume dielectric permittivity and impedance at the lower
495 and upper boundaries of effective WGEI influence remarkably on the VLF losses. The modulation of the electron
496 concentration at the altitudes above z= 120 km affects the excitation of E_y component within the waveguide rather weakly.

5. Influence of the parameters of WGEI on the polarization transformation and losses of the propagating VLF waves

499 An important effect of the gyrotropy and anisotropy is the corresponding transformation of the field polarization

500 during the propagation in the WGEI, which is absent in the ideal metal planar waveguide without gyrotropy and anisotropy.

501 We will show that this effect is quite sensitive to the carrier frequency of the beam, propagating in the WGEI, inclination of

502 the geomagnetic field and perturbations in the electron concentration, which can vary under the influences of the powerful

503 sources placed "below", "above" and "inside" the ionosphere. In the real WGEI, the anisotropy and gyrotropy are connected

504 with the volume effect and effective surface tensor impedances at the lower and upper surfaces of the effective WGEI where

505 z=0 and z= L_z (Fig. 1). For the corresponding transformation of the field polarization determination, we introduce the

506 characteristic polarization relation $|E_y / H_y|(z; y = L_y / 2; x = x_0)$, taken at the central plane of the beam ($y=L_y$) at the

507 characteristic distance ($x=x_0$) from the beam input/VLF transmitter. The choice of the characteristic polarization parameter

508 ($|E_y/H_y|$) and its dependence on the vertical coordinate (z) is justified by conditions (1) – (3). (1) The WGEI is similar to the

509 ideal planar metallized waveguide because, first, the tensor $\hat{\varepsilon}$ is different from the isotropic $\hat{I}$ only in the relatively small

510 upper part of the WGEI in the altitude range from 75-80 to 85 km (see Fig. 1). Second, both the Earth and ionosphere

511 conductivity are quite high and corresponding impedances are quite low. In particular, the elements of the effective tensor

512 impedance at the upper boundary of WGEI are small, $|Z0\alpha\beta| \leq 0.1$ (see, for example, Table 1). (2) Respectively, the carrier

513 modes of the VLF beam are close to the modes of the ideal metallized planar waveguide. These modes are subdivided into

514 the sets of uncoupled (Ex,Hy,Ez) and (Hx,Ey,Hz) modes. The detailed search of the propagation of the separate eigenmodes

515 of the WGEI is not a goal of this paper, and respectively, will be the subject of the separate paper. (3) Because we have

516 adopted for the initial beam(s) the input boundary conditions in the form (32) (with $H_y \neq 0$, $E_y = 0$), the above mentioned

517 value $|E_y / H_y|(z; y = L_y / 2; x = x_0)$ characterizes the mode coupling and corresponding transformation of the polarization

518 at the distance x_0 from the beam input due to the presence of the volume and surface gyrotropy and anisotropy in the real

519 WGEI. The results presented below are obtained for x_0 =1000 km, that is, by the order of value, a typical distance, for

520 example, between the VLF transmitter and receiver of the European VLF/LF radio network (Biagi et al. 2015). Other

521 parameter characterizing the propagation of the beam in the WGEI, the effective total loss parameter is $|H_{ymax}(x=x_0)/$

522 $H_{ymax}(x=0)|$. Note that this parameter characterizes both dissipative and diffraction losses. The last are connected with beam

523 spreading in the transverse (y) direction during the propagation in the WGEI.

524 In Fig. 8 the polarization and loss characteristics dependencies on both the carrier beam frequency and the angle

525 θ between the geomagnetic field and the vertical directions (see Fig. 1) are shown.

(a)   (b)


(c)   (d)
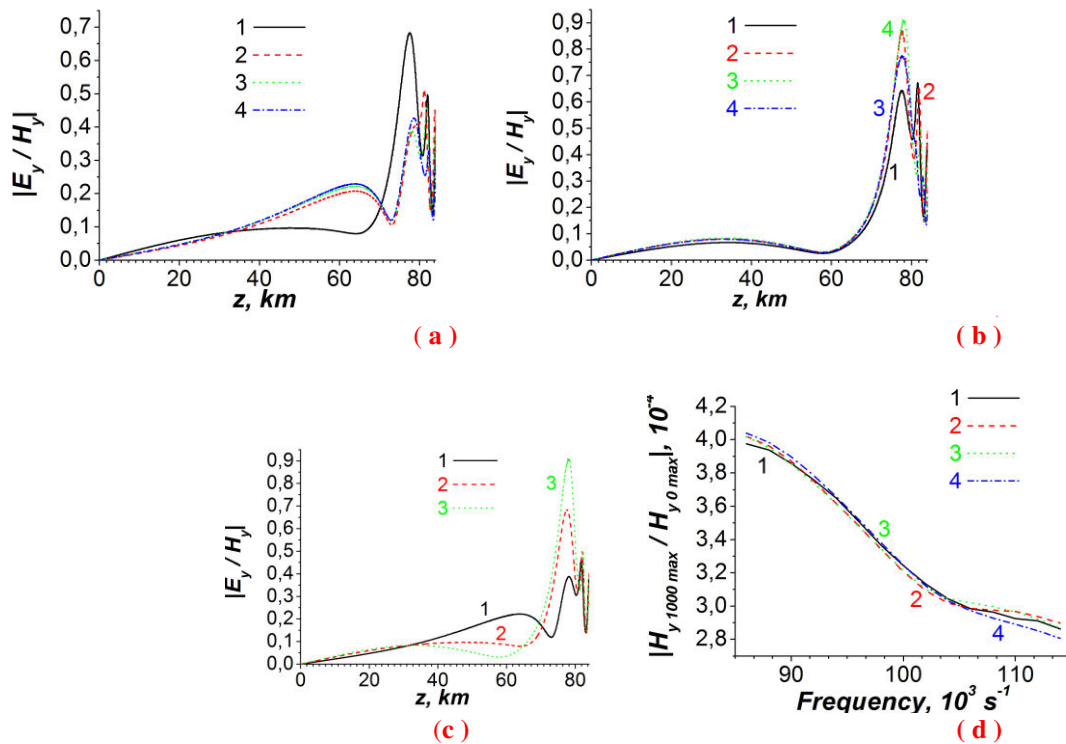
Figure 8. Characteristics of the polarization transformation parameter $|E_y/H_y|$ (a-c) and effective coefficient of the total losses at the distance $x_0=1000$ km from the beam input (d); corresponding altitude dependence of the electron concentration is shown in Fig. 5b line (1); (a, b) and (d) - dependences of the polarization parameter (a, b) and total losses (d) on the vertical coordinate for different angles θ, respectively; black (1), red (2), green (3) and blue (4) curves in Figs. a, b and d correspond to θ equal to $5°, 30°, 45°$ and $60°$, respectively; (a) and (b) correspond to frequencies $\omega = 0.86 \cdot 10^5 s^{-1}$ and $\omega = 1.14 \cdot 10^5 s^{-1}$, respectively; (c) – dependence of the polarization parameter on the vertical coordinate for the different frequencies; black (1), red (2) and green (3) lines correspond to the frequencies $0.86 \cdot 10^5$, $1 \cdot 10^5$ and $1.14 \cdot 10^5$ s^{-1}, respectively and $\theta = 45°$.

537 In Fig. 8a-c the altitude dependence of the polarization parameter |Ey/Hy| exhibits two main maxima in the WGEI. The first

538 one lies in the gyrotropic region above 70 km, while the second one in the isotropic region of the WGEI. As it is seen from

539 Fig. a, b, the value of the (larger) second maximum increases, while the value of the first maximum decreases and its

540 position shifts to the lower altitudes with increasing frequency. At the higher frequency ($\omega = 1.14 \cdot 10^5 c^{-1}$), the larger

541 maximum of the polarization parameter corresponds to the intermediate value of the angle $\theta = 45°$ (Fig. 8 b); for the lower

542 frequency ($\omega = 0.86 \cdot 10^5 c^{-1}$), the largest value of the first (higher) maximum corresponds to the almost vertical direction of

543 the geomagnetic field ($\theta = 5°$, Fig. 8 a). For the intermediate value of the angle ($\theta = 45°$), the largest value of the main

544 maximum corresponds to the higher frequency ($\omega = 1.14 \cdot 10^5 c^{-1}$) in the considered frequency range (Fig. 8 c). The total losses

545 increase monotonically with increasing frequency and depend weakly on the value of θ (Fig. 8 d).

22

546   To model the effect of increasing and decreasing the electron concentration n_e in the lower ionosphere on the

547   polarization parameter, we have used the following parameterization for the n_e change $\Delta n_e = n_e(z) - n_{0e}(z)$ of the electron

548   concentration, where $n_{0e}(z)$ is the unperturbed altitude distribution of the electron concentration:

549     $$\Delta n_e(z) = n_{0e}(z)\Phi(z) \ ; \ \ \Phi(z) = [F(z)] - \frac{(z - z_2)^2}{\Delta z_{12}^2}[F(z_1)] - \frac{(z - z_1)^2}{\Delta z_{12}^2}[F(z_2)] \ ; \ \ F(z) = f_{00} \cdot ch^{-2}\{[z - (\frac{z_1 + z_2}{2})]/\Delta z\} \ (35)$$

550

551   In Eqs. (35), $\Delta z_{12} \equiv z_2 - z_1$; Δz is the effective width of the electron concentration perturbation altitude distribution. The

552   perturbation Δn_e is concentrated in the range of altitudes $z_1 \le z \le z_2$ and is equal to zero outside this region,

553     $\Delta n_e(z_1) = \Delta n_e(z_2) = 0$, while $\Phi(z_1) = \Phi(z_2) = 0$.

554
555
556   **(a)**   **(b)**   **(c)**
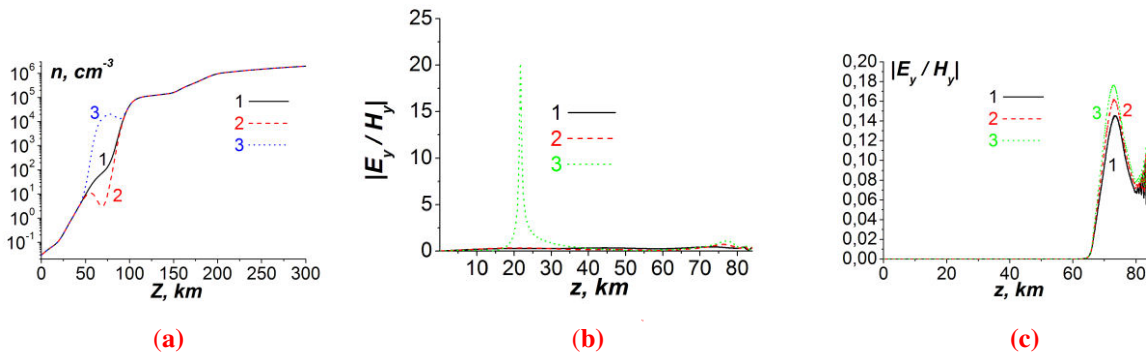
557 **Figure 9. (a) Decreased and increased electron concentration (line 2, red color) and (line 3, blue) correspond to $f_{00} = -1.25$ and**

558 **$f_{00} = 250$, respectively, relative to reference concentration (line 1, black) with parametrization conditions (see Eqs. (35)): $z_1 = 50$**

559 **km, $z_2 = 90$ km, $\Delta z = 20$ km ; (b) and (c) are the polarization parameter $|E_y/H_y|$ altitude distribution, for decreased and increased**

560 **electron concentration, respectively. In (b) and (c) lines 1, 2 and 3 correspond to ω values $0.86 \cdot 10^5 s^{-1}$, $1 \cdot 10^5 s^{-1}$ and**

561 **$1.14 \cdot 10^5 s^{-1}$, respectively. Angle θ is equal to $45°$.**

562   The change in the concentration in the lower ionosphere causes rather nontrivial effect on the parameter of the

563   polarization transformation $|E_y/H_y|$, Fig. 9 a-c. Note that either increase or decrease in the ionosphere plasma concentration

564   have been reported as a result of seismogenic phenomena, tsunamis, particle precipitation in the ionosphere due to wave-

565   particle interaction in the radiation belts (Pulinets et al. 2005; Shinagawa et al. 2013; Arnoldy et al. 1989; Glukhov et al.

566   1992; Tolstoy et al. 1986) etc. The changes in the $|E_y/H_y|$ due to increase or decrease in electron concentration vary by

567   absolute values from dozens to thousands percent, as it is seen from the comparison between Figs. 9b, c (lines 3) and Fig. 8c

568   (line 3), which corresponds to the unperturbed distribution of the ionospheric electron concentration (see also lines 1 in Figs.

569   5b and 9a). It is even more interesting that in the case of decreasing (Fig. 9 a, curve 2) electron concentration, the main

570   maximum of $|E_y/H_y|$ aoppears in the lower atmosphere (at the altitude around 20 km, Fig. 9 b, curve 3, which corresponds to

571     $\omega \blacksquare 1.14 \cdot 10^5 c^{-1}$). In the case of increasing electron concentration (Fig. 9 a, curve 3) the main maximum of $|E_y/H_y|$ appears

572   near the E region of the ionosphere (at the altitude around 77 km, Fig. 9 c). The secondary maximum, which is placed, in the

573 absence of the perturbation of the electron concentration, in the lower atmosphere (Fig. 8 c, curves 2, 3), or

574 mesosphere/ionosphere D region ((Fig. 8 c, curve 1), practically disappears or just is not seen in the present scale, in the case

575 under consideration (Fig. 9 c, curves 1-3).

576

577 a   b   c
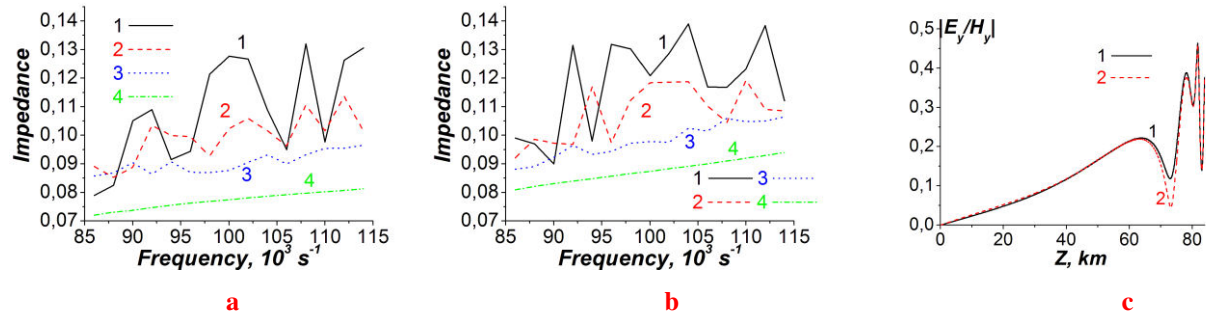
578 **Figure 10. (a, b) Frequency dependencies of the real (a) and imaginary (b) parts of the effective tensor impedance Z_{011} component**
579 **at the upper boundary ($z=L_z$, see Fig. 1) of the WGEI. Lines 1 (black), 2 (red), 3 (blue) and 4 (green) correspond to $\theta = 5°, 30°, 45°$**
580 **and $60°$ degrees respectively; (c) polarization parameter $|E_y/H_y|$ altitude dependency at the frequency $\omega = 0.86 \cdot 10^5$ s^{-1} and angle**
581 **$\theta = 45°$ for the isotropic surface impedance Z_0 at the lower surface of the WGEI equal to 10^{-4}. Earth conductivity σ equal to**
582 **10^9 s^{-1}, line 1 and $Z_0 = 10^{-2}$ ($\sigma = 10^7 s^{-1}$), line 2.**

583

584   In Fig. 10, the real (a) and imaginary (b) parts of the surface impedance at the upper boundary of the WGEI have a

585 quasi-periodical character with the amplitude of oscillations occurring around the effective average values (not shown

586 explicitly in Figs. 10 a, b), which decreases with increasing the angle θ. The average $Re(Z_{011})$ and $Im(Z_{011})$ values in

587 general, decrease with increasing angle θ (see Fig. 10a, b). The average values of $Re(Z_{011})$ at $\theta = 5°, 30°, 45°$ and $60°$ (lines 1-

588 4 in Fig. 10a) and $Im(Z_{011})$ at $\theta = 45°$ and $60°$ (curves 3, 4 in Fig. 10b) increase with increasing frequency in the frequency

589 range $(0.86-1.14) \cdot 10^5$ s^{-1}. The average $Im(Z_{011})$ value at $\theta = 5°$ and $30°$ changes in the frequency range $(0.86-1.14) \cdot 10^5$ s^{-1}

590 non-monotonically with the maximum at $(1-1.1) \cdot 10^5$ s^{-1}. The value of finite impedance at the lower Earth-atmosphere

591 boundary of the WGEI influences on the polarization transformation parameter minimum near the E region of the ionosphere

592 (lines 1, 2 in Fig. 10c). The decrease of surface impedance Z_0 at the lower boundary Earth-atmosphere of the WGEI by two

593 orders of magnitude produces the 100% increase of the corresponding $|E_y/H_y|$ minimum at $Z \sim 75$ km (Fig. 10 c).

594 # 6. Discussion

595   The observations presented in (Rozhnoi et al., 2015), shows a possibility for seismogenic increasing losses of VLF

596 waves in the WGEI (Fig. 11; see details in (Rozhnoi et al. 2015)). We discuss the qualitative correspondence of our results to

597 these experimental data.
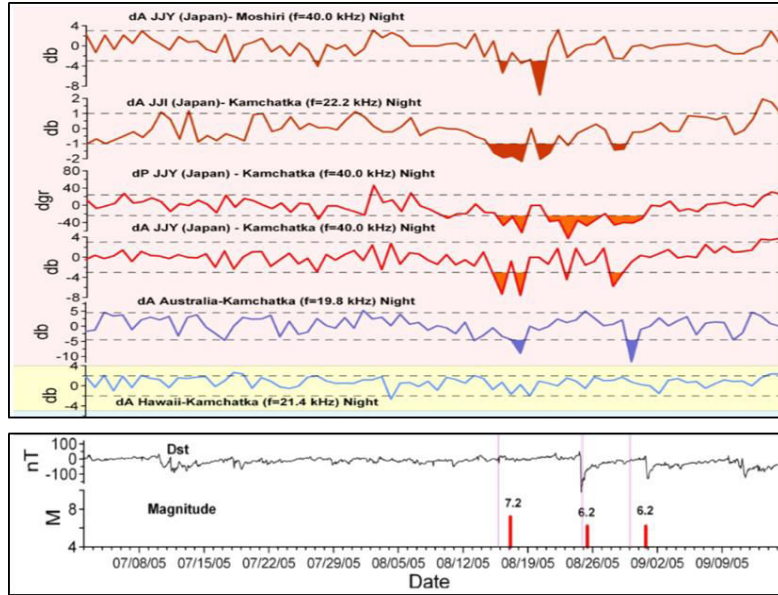
Figure 11. Averaged residual VLF/LF signals from ground-based observations at the wave paths: JJY-Moshiri, JJI-Kamchatka, JJY-Kamchatka, NWC-Kamchatka, and NPM-Kamchatka. Horizontal dotted lines show 2σ level. The color filled zones highlight values exceeding the -2σ level. In panel below Dst variations and earthquakes magnitude values are shown (from Rozhnoi et al., 2015, see their Fig. 1 but not including the DEMETER data; the work of Rozhnoi et al. (2015) is licensed under a Creative Commons Attribution 4.0 International License (CC BY 4.0)). See other details in (Rozhnoi et al., 2015).
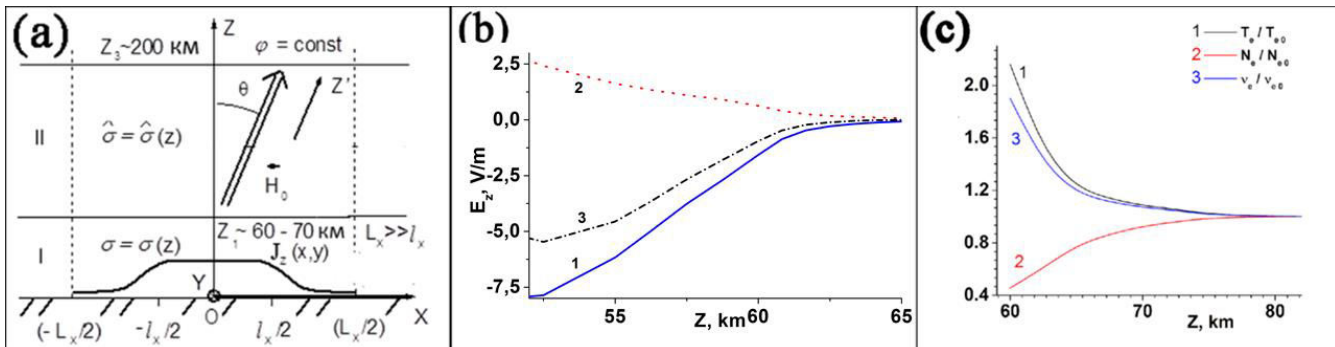
Figure 12. Modification of the ionosphere by electric field of seismogenic origin based on the theoretical model (Rapoport et al. 2006). (a) Geometry of the model for the determination of the electric field excited by seismogenic current source $J_z(x, y)$ and penetrated into the ionosphere with isotropic (I) and anisotropic (II) regions of the system "atmosphere-ionosphere". (b) Electric field in the mesosphere in presence of the seismogenic current sources only in the mesosphere (1); in the lower atmosphere (2); both in the mesosphere and in the lower atmosphere (3). (c) Relative perturbations caused by seismogenic electric field, normalized on the corresponding steady-state values in the absence of perturbing electric field, denoted by the index "0", of electron temperature (T_e / T_{e0}), electron concentration (N_e / N_{e0}), and electron collision frequency (ν_e / ν_{e0}).

25
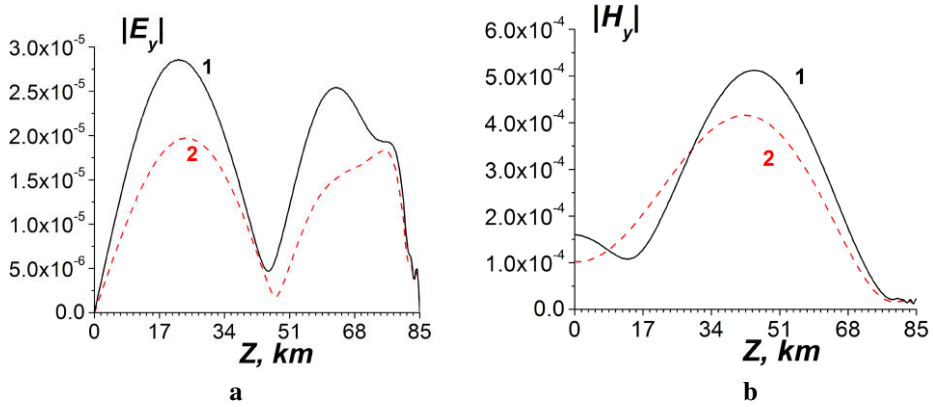
Figure 13. Altitude distributions of the normalized tangential (*y*) electric (a) and magnetic (b) VLF beam field components in the central plane of the transverse beam distribution (*y=0*) at the distance *x=1000* km from the input of the system. Line 1 in (a, b) corresponds to the presence of the mesospheric electric current source only with relatively small value of N_e and large v_e. Line 2 corresponds to the presence of both mesospheric and near-ground seismogenic electric current sources with relatively large value of N_e and small v_e. Lines 1 and 2 in (a, b) correspond qualitatively to the lines 1 and 3, respectively, in Fig. 12b. $\omega = 1.5 \cdot 10^5 s^{-1}$; $\theta = 45°$.

The modification of the ionosphere due to electric field excited by the near-ground seismogenic current source has been taken into account. In the model (Rapoport et al., 2006), the presence of the mesospheric current source, which followed from the observations (Martynenko et al., 2001; Meek et al., 2004; Bragin, 1974) is also taken into account. It is assumed that the mesospheric current has only the Z-component and is positive, which means that it is directed vertically downward, as is the fair-weather current (curve 1, Fig. 12b). Then suppose that the surface seismogenic current is directed in the same way as the mesospheric current. We first consider the case when the mesospheric current is zero and only the corresponding seismogenic current is present near the earth. The corresponding mesospheric electric field under the condition of a given potential difference between the Earth and the ionosphere (curve 2, Fig. 12 b) is directed opposite to those excited by the corresponding mesospheric current (curve 1, Fig. 12 b). As a result, in the presence of both mesospheric and a seismogenic surface current, the total mesospheric electric field (curve 3, Fig. 12 b) is smaller in absolute value than in the presence of only a mesospheric current (curve 1, Fig. 12 b). It has been shown by Rapoport et al., (2006) that the decrement of losses $|k''|$ for VLF waves in the WGEI is proportional to $|k''| \sim |\varepsilon''| \sim N_e / v_e$. N_e and v_e decrease and increase, respectively, due to the appearance of a seismogenic surface electric current, in addition to the mesospheric current (curve 3, Fig. 12, b). As a result, the losses increase compared with the case when the seismogenic current is absent and the electric field has a larger absolute value (curve 1, Fig. 12). The increase in losses in the VLF beam, shown in Fig. 13 (compare curves 2 and 1 in Figs. 13 a, b) corresponds to an increase in losses with an increase in the absolute value of the imaginary part of the dielectric constant, when a near-surface seismogenic current source appears (curve 3 in Fig. 12 b), in addition to the existing mesospheric current source (curve 2 in Fig. 12 b). This seismogenic increase in losses corresponds qualitatively to the results, presented in (Rozhnoi et al. 2015).

26

The TIMEB is a new method of modeling characteristics of the WGEI. The results of beam propagation in WGEI modeling presented above include the range of altitudes inside the WGEI (see Figs. 4-7). Nevertheless, the TIMEB method described by Eqs. (15)-(19), (22-24), (27), (30) and allows to determine all field components in the range of altitudes $0 \leq z \leq L_{max}$, where $L_{max} = 300$ km. The structure and behavior of these eigenmodes in the WGEI and leakage waves will be a subject of separate papers. We present here only the final qualitative result of the simulations. In the range $L_z \leq z \leq L_{max}$, where $L_z = 85$ km is the upper boundary of the effective WGEI, all field components are (1) at least one order of altitude less than the corresponding maximal field value in the WGEI and (2) field components have the oscillating character along z coordinate and describe the modes, leaking from the WGEI.

Let us make a note also on the dependences of the field components in the WGEI on the vertical coordinate (z). The initial distribution of the electromagnetic field with altitude z (Fig. 4a) is determined by the boundary conditions of the beam (see Eq. (32)). The field component includes higher eigenmodes of the WGEI. The higher-order modes experienced quite large losses and practically disappear after beam propagation on 1000 km distance. This determines the change in altitude (z) and transverse (y) distributions of the beam field during propagation along the WGEI. In particular, at the distance x=600 km from the beam input (Figs. 4b, c), the few lowest modes of the WGEI along z and y coordinates still persist. At distance x=1000 km (Fig. 4d, c; Fig. 6e, f; and Fig. 7a, b), only the main mode persists in the z direction. Note, the described field structure correspond to real WGEI with losses. The gyrotropy and anisotropy causes the volume effects and surface impedance, in distinction to the ideal planar metallized waveguide with isotropic filling (Collin, 2001).

The closest approach of the direct investigation of the VLF electromagnetic field profile in the Earth-Ionosphere waveguide was a series of sounding rocket campaigns at mid- and high-latitudes at Wallops Is., VA and Siple Station in Antarctica (Kintner et al., 1983; Brittain et al., 1983; Siefring and Kelly, 1991; Arnoldy and Kintner, 1989), where single-axis E-field and three-axis B-field antennas, supplemented in some cases with in situ plasma density measurements were used to detect the far-field fixed-frequency VLF signals radiated by US Navy and Stanford ground transmitters.

The most comprehensive study of the WGEI will be provided by the ongoing NASA VIPER (VLF Trans-Ionospheric Propagation Experiment Rocket) project (PI J. W. Bonnell, UC Berkeley, NASA Grant 80NSSC18K0782). The VIPER sounding rocket campaign is consist of a summer nighttime launch during quiet magnetosphere conditions from Wallops Flight Facility, VA, collecting data through the D, E, and F regions of the ionosphere with a payload carrying the following instrumentation: 2D E- and 3D B-field waveforms, DC-1 kHz; 3D ELF to VLF waveforms, 100 Hz to 50 kHz; 1D wideband E-field measurement of plasma and upper hybrid lines, 100 kHz to 4 MHz; and Langmuir probe plasma density and ion gauge neutral density measurements at a sampling rate of at least tens of Hz. The VIPER project will fly a fully 3D EM field measurement, DC through VLF, and relevant plasma and neutral particle measurements at mid-latitudes through the radiation fields of (1) an existing VLF transmitter (the VLF transmitter Cutler with call sign NAA, the very low frequency (VLF) shore radio station at Cutler, Maine, USA, which transmits, at a frequency of 24 kHz an input power of up to 1.8 megawatts, see Fig. 11) and (2) naturally-occurring lightning transients through and above the leaky upper boundary of the WGEI supported by a vigorous theory and modeling effort in order to explore the vertical and horizontal profile of the

675 observed 3D electric and magnetic radiated fields of the VLF transmitter, and the profile related to the observed plasma and
676 neutral densities. The VLF wave's reflection, absorption, and transmission processes as a function of altitude will be
677 searched making use of the data on the vertical VLF E- and B-field profile.
678
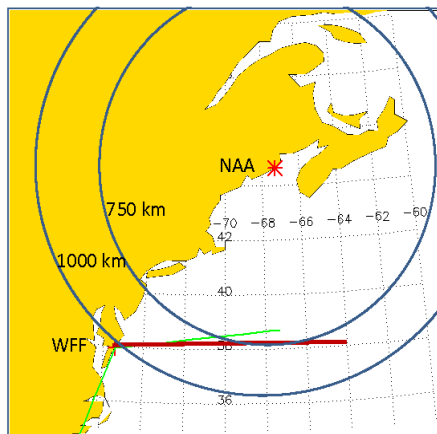
679
680 **Figure 14. Proposed VIPER Trajectory**
681
682 The aim of this experiment will be the investigation of the VLF beams launched by the near-ground source/VLF transmitter
683 with the known parameters and propagating both in the WGEI and leaking from WGEI into the upper ionosphere.
684 Characteristics of these beams will be compared with the theory proposed in the present paper and the theory on leakage of
685 the VLF beams from WGEI, which we will present in the next papers.
686

687 **Conclusions**

688   (1) We have developed the new and highly effective robust method of tensor impedance for the VLF electromagnetic
689 beam propagation in the inhomogeneous waveguiding media – the "tensor impedance method for modeling propagation of
690 electromagnetic beams (TIMEB)" in a multi-layered/inhomogeneous waveguide. The main differences/advantages of the
691 proposed tensor impedance method in comparison with the known method of the impedance recalculating, in particular
692 invariant imbedding methods (Shalashov and Gospodchikov, 2010; Kim and Kim, 2016) are the following: (i) our method is
693 a direct method of the recalculation of tensor impedance, and the corresponding tensor impedance is determined analytically,
694 (see Eq. (22)); (ii) our method applied for the media without non-locality does not need a solution of integral equation(s), as
695 the invariant imbedding method; (iii) the proposed tensor impedance method does not need the revealing the forward and
696 reflected waves. Moreover, even the conditions of the radiation in Eq. (12) at the upper boundary $z=L_{max}$ is determined
697 through the total field components $H_{x,y}$ that makes the proposed procedure technically less cumbersome and practically more
698 convenient.

28

(2) The waveguide includes the region for the altitudes 0 < z < 80 - 90 km. The boundary conditions are the radiation conditions at $z = 300$ km, which can be recalculated to the lower altitudes as the tensor relations between the tangential components of the EM field. In another words, the tensor impedance conditions have been used at $z = 80 – 90$ km.

(3) The application of this method jointly with the previous results of the modification of the ionosphere by seismogenic electric field gives the results, which qualitatively are in agreement with the experimental data on the seismogenic increasing losses of VLF waves/beams propagating in the WGEI.

(4) The observable qualitative effect is mutual transformation of different polarizations of the electromagnetic field occur during the propagation. This transformation of the polarization depends on the electron concentration, i.e. the conductivity, of D- and E-layers of the ionosphere at the altitudes 75 – 120 km.

(5) Changes in complex tensors of both volume dielectric permittivity and impedances at the lower and upper boundaries of effective WGEI influence remarkably on the VLF losses in the WGEI.

(6) An influence is demonstrated on the parameters characterizing the propagation of the VLF beam in the WGEI, in particular, on the parameter of the transformation polarization $|E_y/H_y|$ and tensor impedance at the upper boundary of the effective WGEI, of the carrier beam frequency, inclination of the geomagnetic field and the perturbations in the altitude distribution of the electron concentration in the lower ionosphere

(i)   The altitude dependence of the polarization parameter $|E_y/H_y|$ has two main maxima in the WGEI: the higher maximum is in the gyrotropic region above 70 km, while the other is in the isotropic region of the WGEI. The value of the (larger) second maximum increases, while the value of the first maximum decreases and its position shifts to the lower altitudes with increasing frequency. In the frequency range of $\omega = (0.86 - 1.14) \cdot 10^5 s^{-1}$,At the higher frequency, the larger maximum polarization parameter corresponds to the intermediate value of the angle $\theta = 45°$; for the lower frequency, the largest value of the first (higher) maximum corresponds to the nearly vertical direction of the geomagnetic field. The total losses increase monotonically with increasing frequency and depend weakly on the value of θ (Fig. 1).

(ii) The change in the concentration in the lower ionosphere causes rather nontrivial effect on the parameter of polarization transformation $|E_y/H_y|$. This effect does include the increase and decrease of the maximum value of the polarization transformation parameter $| E_y/H_y |$. The corresponding change of this parameter has large values from dozens to thousands percent. In the case of decreasing electron concentration, the main maximum of $|Ey/Hy|$ appears in the lower atmosphere at an altitude of around 20 km. In the case of increasing electron concentration, the main maximum of $| E_y/H_y|$ appears near the E region of the ionosphere (at the altitude around 77 km), while the secondary maximum practically disappears.

(iii) The real and imaginary parts of the surface impedance at the upper boundary of the WGEI have a quasi-periodical character with the amplitude of "oscillations" occurring around some effective average values decreases with increasing the angle θ. Corresponding average values of $Re(Z_{11})$ and $Im(Z_{11})$, in general, decrease with

29

732   increasing angle θ. Average values of $Re(Z_{11})$ for θ equal to $5°, 30°, 45°$ and $60°$ and $Im(Z_{11})$ corresponding to θ

733   jio equal to $45°$ and $60°$, increase with increasing frequency in the considered frequency range $(0.86\text{-}1.14)\cdot 10^5$ s^{-1}.

734   The average value of $Im(Z_{11})$ corresponds to θ equal to $5°$ and $30°$, change in the frequency range $(0.86\text{-}1.14)\cdot 10^5$ s$^-$

735   ^{1} non-monotonically, having maximum values around frequency $(1\text{-}1.1)\cdot 10^5$ s^{-1}.

736   (iv) The value of finite impedance at the lower Earth-atmosphere boundary of the WGEI make quite observable

737   influence on the polarization transformation parameter minimum near the E region of the ionosphere. The decrease

738   of surface impedance Z at the lower boundary Earth-atmosphere of the WGEI in two orders causes the increase of

739   the corresponding minimum value of $|E_y/H_y|$ in ~ 100%.

740   (7) In the range $L_z \leq z \leq L_{max}$, where $L_z = 85$ km is the upper boundary of the effective WGEI, all field components are

741   (a) at least one order of altitude less than the corresponding maximal value in the WGEI, and (b) field components have the

742   oscillating character (along the z coordinate) and describes the modes, leaking from the WGEI. The detail consideration of

743   the electromagnetic waves leaking from the WGEI will be presented in the separate paper. The initial distribution of the

744   electromagnetic field with z (vertical direction) is determined by the initial conditions on the beam. This field includes

745   higher eigenmodes of the WGEI. The higher-order modes, in distinction to the lower ones, have quite large losses and

746   practically disappear after a beam propagation for 1000 km distance. This circumstance determines the change in altitude (z)

747   distribution of the field of the beam during its propagation along the WGEI. In particular, at the distance x = 600 km from

748   the beam input, the few lowest modes of the WGEI along z coordinates are still survived. Further, at x=1000 km, practically,

749   only the main mode in the z direction remains. This fact reflects in a minimum number of oscillations of the beam field

750   components along z at a given value of x.

751   (8) The proposed propagation of VLF electromagnetic beams in the WGEI model and results will be useful to explore

752   the characteristics of these waves as an effective instrument for diagnostics of the influences on the ionosphere "from above"

753   in the system of Sun-Solar Wind-Magnetosphere-Ionosphere, "from below" from the most powerful meteorological,

754   seismogenic and other sources in the lower atmosphere and lithosphere/Earth, such as hurricanes, earthquakes, tsunamis, and

755   from inside the ionosphere by the strong thunderstorms with lightning discharges, and even from the far space by as gamma-

756   flashes, cosmic rays events.

757

OA. JB and GM took part in developing the concept of the paper, and writing the initial version of the paper. OA, GM, VF, AG contributed to the preparation of the revised version of the paper.

All participants took part in the analysis of the results.

COMPETING INTERESTS

The authors declare that they have no conflict of interest.

DATA AVAILABILITY

The VLF–LF data (Fig. 11) are property of IPE and TUoS groups, and they are not publicly accessible. According to an agreement between all the participants, we cannot make the data openly accessible. Data can be provided under commercial conditions via direct request to rozhnoi@ifz.ru. The ionospheric data used for the modeling the electrodynamics characteristics of the VLF waves in the ionosphere are shown in part in Fig. 5 (namely, altitude distribution of electron concentration). The other data necessary for determination the components of tensor of dielectric permittivity and then the electrodynamics modeling in the accepted simple approximation of the three-component plasma-like ionosphere (including electron, one effective ion and one effective neutral components) and quasi-neutrality are mentioned in Sect. 3.1. The corresponding ionospheric data have been taken from the well-known published handbooks, referred in the paper (Al'pert 1972; Alperovich and Fedorov 2007; Kelley 2005; Schunk and Nagy 2010; Jursa 1985).

REFERENCES

Agapitov, O. V., Artemyev, A. V., Mourenas, D., Kasahara, Y., and Krasnoselskikh, V.: Inner belt and slot region electron lifetimes and energization rates based on AKEBONO statistics of whistler waves, J. Geophys. Res.: Space Phys., 119, 2876–2893, https://doi.org/10.1002/2014JA019886, 2014.

Agapitov, O. V., Mourenas, D., Artemyev, A. V., Mozer, F. S., Hospodarsky, G., Bonnell, J., and Krasnoselskikh, V: Synthetic Empirical Chorus Wave Model From Combined Van Allen Probes and Cluster Statistics, J. Geophys. Res.: Space Phys., 123, 2017JA024843, https://doi.org/10.1002/2017JA024843, 2018.

Alperovich, L. S. and Fedorov, E. N.: Hydromagnetic Waves in the Magnetosphere and the Ionosphere, Springer, 426 pp., 2007.

31

798   Al'pert, Ya.L: Propagation of Electromagnetic Waves and the Ionosphere (in Russian), Moscow, Nauka Publ., 1972, 563 pp

799   Arnoldy, R. L. and Kintner, P. M.: Rocket observations of the precipitation of electrons by ground VLF transmitters, J.

800   Geophys. Res.: Space Phys., 94, 6825–6832, https://doi.org/10.1029/JA094iA06p06825, 1989.

801   Artsimovich, L. A. and Sagdeev, R. Z: Physics of plasma for physicists, ATOMIZDAT Publ. House, Moscow, 320 pp., 1979

802   (in Russian).

803   Artemyev, A. V., Agapitov, O. V., Mourenas, D., Krasnoselskikh, V., and Zelenyi, L. M.: Storm-induced energization of

804   radiation belt electrons: Effect of wave obliquity, Geophys. Res. Lett., 40, 4138–4143, https://doi.org/10.1002/grl.50837,

805   2013.

806   Artemyev, A., Agapitov, O., Mourenas, D., Krasnoselskikh, V., and Mozer, F.: Wave energy budget analysis in the Earth's

807   radiation belts uncovers a missing energy, Nat. Commun., 6, https://doi.org/10.1038/ncomms8143, 2015.

808   Azadifar, M., Li, D., Rachidi, F., Rubinstein, M., Diendorfer, G., Schulz, W., Pichler, H., Rakov, V. A., Paolone, M.,

809   Pavanello, D.: Analysis of lightning-ionosphere interaction using simultaneous records of source current and 380-km distant

810   electric field, Journ. Atmos. Solar-Terrestr. Phys., 159, 48–56, https://doi.org/10.1016/j.jastp.2017.05.010, 2017.

811   Beletskii, N. N., Borysenko, S. A., and Gvozdev, N. I.: The Resonant Interaction of Electromagnetic Waves in a Defect

812   Dielectric Periodic Layered Structure Placed in a Parallel-Plate Waveguide, Radiophys. Electron., 5, 7 pp.,

813   https://doi.org/10.1615/TelecomRadEng.v75.i6.40, 2014.

814   Biagi, P. F., Maggipinto, T., and Ermini, A.: The European VLF/LF radio network: current status, Acta Geod. Geophys., 50,

815   109–120, https://doi.org/10.1007/s40328-014-0089-x, 2015.

816   Biagi, P. F., Maggipinto, T., Righetti, F., Loiacono, D., Schiavulli, L., Ligonzo, T., Ermini, A., Moldovan, I. A., Moldovan,

817   A. S., Buyuksarac, A., Silva, H. G., Bezzeghoud ,M., and Contadakis, M. E.: The European VLF/LF radio network to search

818   for earthquake precursors: setting up and natural/man-made disturbances, Nat. Hazards Earth Syst. Sci., 11, 333–341,

819   https://doi.org/10.5194/nhess-11-333-2011, 2011.

820   Boudjada, M. Y., Schwingenschuh, K., Al-Haddad, E., Parrot, M., Galopeau, P. H. M., Besser, B., Stangl, G., and Voller,

821   W., Effects of solar and geomagnetic activities on the sub-ionospheric very low frequency transmitter signals received by the

822   DEMETER micro-satellite, Ann. Geo., 55, 1, https://doi.org/10.4401/ag-5463, 2012.

823   Bragin, Yu. A., Tyutin Alexander, A., Kocheev, A.A., and Tyutin, Alexei, A.: Direct measurements of the vertical electric

824   field of the atmosphere up to 80 km, Space Res., 12, 279–281, 1974.

825   Brittain, R., Kintner, P. M., Kelley, M. C., Siren, J. C., and Carpenter, D. L.: Standing wave patterns in VLF Hiss, J.

826   Geophys. Res.: Space Phys., 88, 7059–7064, https://doi.org/10.1029/JA088iA09p07059, 1983.

827   Buitink, S., Corstanje, A., Enriquez, J. E., Falcke, H., Hörandel ,J. R., Huege, T., Nelles, A., Rachen, J. P., Schellart, P.,

828   Scholten, O., ter Veen, S., Thoudam, S., and Trinh, T. N. G.: A method for high precision reconstruction of air shower X_{max}

829   using two-dimensional radio intensity profiles, arXiv:1408.7001v2 [astro-ph.IM], 1 Sep 2014.

830   Chevalier, M. W., Inan U. S.: A Technique for Efficiently Modeling Long-Path Propagation for Use in Both FDFD and

831   FDTD, IEEE Ant. Wireless Propag. Lett., 5, 525-528, https://doi.org/10.1109/LAWP.2006.887551, 2006

832 Chou, M.-Y., Lin, C. C. H., Yue, J., Chang, L. C., Tsai, H.-F., and Chen, C.-H., Medium-scale traveling ionospheric

833 disturbances triggered by Super Typhoon Nepartak, Geophys. Res. Lett., 44, 7569–7577,

834 https://doi.org/10.1002/2017gl073961, 2017.

835 Collin, R. E., *Foundations for Microwave Engineering*. New York: John Willey & Sons, Inc., 2001.

836 Cummer, S. A., Inan ,U. S., Bell, T. F., and Barrington-Leigh, C. P.: ELF radiation produced by electrical currents in sprites,

837 Geophys. Res. Lett., 25, 1281–1284, https://doi.org/10.1029/98GL50937, 1998.

838 Cummer, S. A., Briggs, M. S., Dwyer, J. R., Xiong, S., Connaughton, V., Fishman, G. J., Lu, G., Lyu, F., and Solanki, R.:

839 The source altitude, electric current, and intrinsic brightness of terrestrial gamma ray flashes, Geophys. Res. Lett., 41,

840 https://doi.org/10.1002/2014GL062196, 2014.

841 Dwyer, J. R. and Uman, M. A.: The physics of lightning, Phys. Rep., 534, 147–241,

842 https://doi.org/10.1016/j.physrep.2013.09.004, 2014.

843 Dwyer, J. R.: The relativistic feedback discharge model of terrestrial gamma ray flashes, Journ. Geophys. Res., 117,

844 A02308, https://doi.org/10.1029/2011JA017160, 2012

845 Glukhov, V. S., Pasko, V. P., & Inan, U. S. (1992). Relaxation of transient lower ionospheric disturbances caused by

846 lightning-whistler-induced electron precipitation bursts. *Journal of Geophysical Research, 97(A11),*

847 *16971*.doi:10.1029/92ja01596

848 Grimalsky, V.V., Kremenetsky, I.A., Rapoport, Yu.G.: Excitation of electromagnetic waves in the lithosphere and their

849 penetration into ionosphere and magnetosphere, J. of Atmosph. Electricity,19, 101-117, 1999 a.

850 Grimalsky, V.V., Kremenetsky, I.A., Rapoport, Yu.G.: Excitation of EMW in the lithosphere and propagation into

851 magnetosphere . In: "Atmospheric and Ionospheric Electromagnetic Phenomena Associated with Earthquakes". Ed.: M.

852 Hayakawa. (TERRAPUB), Tokyo, 777-787, 1999 b.

853 Guglielmi A.V., Pokhotelov O.A.: *Geoelectromagnetic waves*. IOP Publ.: Bristol, 1996, 402 P.

854 Gurevich, A V, Zybin, K P.: Runaway breakdown and electric discharges in thunderstorms, Physics – Uspekhi, 44, 11, 1119

855 – 1140, https://doi.org/10.1070/PU2001v044n11ABEH000939, 2001

856 Gurevich, A V., Karashtin, A N., Ryabov, V A., Chubenko, A L Shepetov: Nonlinear phenomena in the ionospheric

857 plasma.Effects of cosmic rays and runaway breakdown on thunderstorm discharges, Physics - Uspekhi 52 (7), 735-745,

858 https://doi.org/0.3367/UFNe.0179.200907h.0779, 2009

859 Hapgood, M.: Space Weather, IOP Publ., Bristol, 23 PP., https://doi.org/10.1088/978-0-7503-1372-8, 2017

860 Hare, B. M., Scholten, O., Bonardi, A., Buitink, S., Corstanje, A., Ebert, U., Falcke, H., Hörandel, J. R., Leijnse, H., Mitra,

861 P., Mulrey, K., Nelles, A., Rachen, J. P., Rossetto, L., Rutjes, C., Schellart, P., Thoudam, S., Trinh, T. N. G., ter Veen, S.,

862 and Winchen, T., LOFAR Lightning Imaging: Mapping Lightning With Nanosecond Precision, J. Geophys. Res.:

863 Atmospheres, 123, 2861–2876, https://doi.org/10.1002/2017JD028132, 2018.

864 Hayakawa, M.: Earthquake prediction with radio techniques, Wiley, Singapore, 294 P., 2015.

Horne, R. B., Thorne, R. M., Shprits, Y. Y., Meredith, N. P., Glauert, S. A., Smith, A. J., Kanekal, S. G.,Baker, D. N., Engebretson, M. J., Posch, J. L., Spasojevic, M., Inan, U. S., Pickett, J. S., and Decreau, P. M. E.: Wave acceleration of electrons in the Van Allen radiation belts. Nature, 437, 227–230, https://doi.org/10.1038/nature03939, 2005

Jursa A.S., Ed.: Handbook of Geophysics and the Space Environment Air Force Geophyics Lab., 1042 P, 1985

Kelley, M. C.: The Earth's Ionosphere Plasma Physics and Electrodynamics, Acad. Press, Amsterdam, 556 P., 2009

Kim, S. and Kim, K.: Invariant imbedding theory of wave propagation in arbitrarily inhomogeneous stratified bi-isotropic media, J. Opt. 18, 065605 (9pp), https://doi.org/10.1088/2040-8978/18/6/065605, 2016.

Kintner, P. M., Brittain, R., Kelley, M. C., Carpenter, D. L., and Rycroft, M. J., In situ measurements of transionospheric VLF wave injection, J. Geophys. Res.: Space Phys., 88, 7065–7073, https://doi.org/10.1029/JA088iA09p07065, 1983.

Kong, J. A., Electromagnetic Wave Theory, New York: John Willey & Sons, Inc., 1990.

Koskinen, H. E. J., Physics of Space Storms. From the Solar Surface to the Earth, Springer-Verlag, 419 P., 2011.

Kurushin, E. P. and Nefedov E. I.: Electrodynamics of anisotropic waveguiding structures, Moscow: Nauka (Science), 1983 (in Russian).

Kuzichev, I.V., Shklyar, D.R.: On full-wave solution for VLF waves in the near-Earth space, Journ. Atmos. Solar-Terrestr. Phys., 72 , 1044–1056, https://doi.org/10.1016/j.jastp.2018.07.002, 2010

Kuzichev, I.V., Vasko, I. Yu., Malykhin, A. Yu., Soto-Chavez, A. R.: On the ionospheric propagation of VLF waves generated by currents in the lower ionosphere, Journ. Atmos. Solar-Terrestr. Phys., 179, 138-148, https://doi.org/10.1016/j.jastp.2018.07.002, 2018

Lehtinen, N. G., Inan U. S.: Radiation of ELF/VLF waves by harmonically varying currents into a stratified ionosphere with application to radiation by a modulated electrojet, Journ Geophys. Res., 113, A06301, https://doi.org/10.1029/2007JA012911, 2008

Lehtinen, N. G., Inan U. S.: Full-wave modeling of transionospheric propagation of VLF waves, Geophys. Res. Lett., 36, L03104, https://doi.org/10.1029/2008GL036535, 2009

Levy, M.: Parabolic equation methods for electromagnetic wave propagation, The Inst. of Electrical Eng., Padstow, Cornwall, 336 P., 2000

Lu, G., Zhang, H., Cummer, S. A., Wang, Y., Lyu, F., Briggs, M., Xiong, S., Chen, A.: A comparative study on the lightning sferics associated with terrestrial gamma-ray flashes observed in Americas and Asia, Journ. Atmos. Solar-Terrestr. Phys. 183, 67–75, https://doi.org/10.1016/j.jastp.2019.01.001, 2019

Maier, S. A.: Plasmonics: Fundamentals and Applications, N. Y.: Springer, 234 p., 2007.

Marshall, R. A., Wallace, T.: Finite-Difference Modeling of Very-Low-Frequency Propagation in the Earth-Ionosphere Waveguide, IEEE Trans. Ant. Propag., 65, 7185-7197, https://doi.org/10.1109/TAP.2017.2758392, 2017

Martynenko, S. I., Rozumenko, V. T., and Tyrnov, O. F.: New possibilities for mesospheric electricity diagnostics, Adv. Space Res., 27, 1127–1132, https://doi.org/10.1016/S0273-1177(01)00208-3, 2001.

Meek, C. E., Manson, A. H., Martynenko, S. I., Rozumenko, V. T., and Tyrnov, O. F.: Remote sensing of mesospheric electric fields using MF radars, J. Atmos. Sol.-Terr. Phys., 66, 881–890, https://doi.org/10.1016/j.jastp.2004.02.002, 2004.

Mezentsev, A., Lehtinen, N., Ostgaard, N., Perez-Invernon, F. J., and Cummer, S. A.: Spectral characteristics of VLF sferics associated with RHESSI TGFs, J. Geophys. Res.: Atmospheres, 123, https://doi.org/10.1002/2017JD027624, 2018.

Nina, A., Radovanović, M., Milovanović, B., Kovačević, A., Bajčetić, J., and Popović, L. C.: Low ionospheric reactions on tropical depressions prior hurricanes, Adv. Space Res., 60, 1866–1877, https://doi.org/10.1016/j.asr.2017.05.024, 2017.

Qin, J., Celestin, S., and Pasko, V. P.: Low frequency electromagnetic radiation from sprite streamers, Geophys. Res. Lett., 39, L22803, https://doi.org/10.1029/2012GL053991, 2012.

Patra, S., Spencer, E. Horton, W. and Sojka, J.: Study of Dst/ring current recovery times using the WINDMI model, Journ. Geophys. Res., 116, A02212, https://doi.org/10.1029/2010JA015824, 2011

Pulinets S and Boyarchuk K (2005) Ionospheric Precursors of Earthquakes, Berlin, Springer, 315P

Rapoport, Yu. G., Boardman, A. D., Grimalsky, V. V., Ivchenko, V. M., Kalinich, N: Strong nonlinear focusing of light in nonlinearly controlled electromagnetic active metamaterial field concentrators, J. Opt. (United Kingdom), 16, 0552029–0552038, https://doi.org/10.1088/2040-8978/16/5/055202, 2014.

Rapoport, Yu. G., Gotynyan, O. E., Ivchenko, V. N., Hayakawa, M., Grimalsky, V. V., Koshevaya, S. V., Juarez, D.: Modeling electrostatic – photochemistry seismoionospheric coupling in the presence of external currents, Phys. Chem. Earth, 31, 4-9, 437–446, https://doi.org/10.1016/j.pce.2006.02.010, 2006

Richmond, A. D.: Space Weather Research Prompts Study of Ionosphere and Upper Atmospheric Electrodynamics, EOS, Trans. , Amer. Geophys. Union, 77,(11), 101, https://doi.org/10.1029/96eo00066, 1996

Rozhnoi, A., Solovieva, M., Levin, B., Hayakawa, M., and Fedun, V.: Meteorological effects in the lower ionosphere as based on VLF/LF signal observations, Nat. Hazards Earth Syst. Sci., 14, 2671–2679, https://doi.org/10.5194/nhess-14-2671-2014, 2014.

Rozhnoi, A., Solovieva, M., Parrot, M., Hayakawa, M., Biagi, P.-F., Schwingenschuh, K., Fedun, V.: VLF/LF signal studies of the ionospheric response to strong seismic activity in the Far Eastern region combining the DEMETER and ground-based observations, Phys. Chem. Earth, 85–86, 141–149, https://doi.org/10.1016/j.pce.2015.02.005, 2015.

Ruibys, G., & Tolutis, R: Nonreciprocal HF signal transmission by surface helicon. Electronics Letters, 19(8), 273. https://doi.org/10.1049/el:19830191, 1983

Samarskii, A.A.: The Theory of Difference Schemes, Marcel Dekker, N.Y., 2001.

Sanchez-Dulcet, F., Rodriguez-Bouza M., Silva, H. G., Herraiz, M., Bezzeghoud, M., Biagi, P. F.: Analysis of observations backing up the existence of VLF and ionospheric TEC anomalies before the Mw6.1 earthquake in Greece, January 26, 2014, Phys. Chem. Earth, 85–86, 150–166, https://doi.org/10.1016/j.pce.2015.07.002, 2015.

Scholten, O., Bonardi, A., Buitink, S., Corstanje, A., Ebert, U., Falcke, H., Hörandel, J., Mitra, P., Mulrey, K., Nelles, A., Rachen, J., Rossetto, L., Rutjes, C., Schellart, P., Thoudam, S., Trinh, G., ter Veen, S., and Winchen, T. Precision study of

radio emission from air showers at LOFAR, EPJ Web of Conferences, 136, 02012, https://doi.org/10.1051/epjconf/201713602012, 2017.

Senior, T. B. A. and J. L. Volakis: Approximate boundary conditions in electromagnetics, London: Institution of Electrical Engineers, 1995.

Shalashov, A. G. and Gospodchikov, E. D.: Impedance technique for modeling electromagnetic wave propagation in anisotropic and gyrotropic media, Physics-Uspekhi, 54, 145–165, https://doi.org/10.3367/UFNe.0181.201102c.0151, 2011.

Siefring, C. L. and Kelley, M. C.: Analysis of standing wave patterns in VLF transmitter signals: Effects of sporadic E layers and in situ measurements of low electron densities, J. Geophys. Res.: Space Phys., 96, 17813–17826, https://doi.org/10.1029/91JA00615, 1991.

Shinagawa, H., Tsugawa, T., Matsumura, M., Iyemori, T., Saito, A., Maruyama, T., … Otsuka, Y. (2013). Two-dimensional simulation of ionospheric variations in the vicinity of the epicenter of the Tohoku-oki earthquake on 11 March 2011. *Geophysical Research Letters, 40(19), 5009–5013.* doi:10.1002/2013gl057627

Schunk, R.W. and Nagy, A.F.: Ionospheres. Physics, Plasma Physics, and Chemistry, Cambridge, CUP, 628 P., 2010

Spiegel, M. R.: Theory and problems of vector analysis and an introduction to tensor analysis, Shnaum Publ., NY, 223 P., 1959.

Surkov, V. and Hayakawa, M.: Ultra and Extremely Low Frequency Electromagnetic Fields, Springer, Tokyo, 2014.

Tarkhanyan, R. H. and Uzunoglu, N. K., Radiowaves and Polaritons in Anisotropic Media, Weinheim: Wiley-VCH, 210 p., 2006.

Thorne, R. M.: Radiation belt dynamics: The importance of wave-particle interactions, Geophys. Res. Lett., 372, 22107, https://doi.org/10.1029/2010GL044990, 2010.

Tolstoy, A., Rosenberg, T. J., Inan, U. S., & Carpenter, D. L. (1986). Model predictions of subionospheric VLF signal perturbations resulting from localized, electron precipitation-induced ionization enhancement regions. *Journal of Geophysical Research, 91(A12), 13473.* doi:10.1029/ja091ia12p13473

Tretyakov, S.: Analytical Modeling in Applied Electromagnetics, Artech House, Boston, 2003.

Walker, A.D. M.: The Theory of Whistler Propagation, Rev. Geophys. Space Phys., 14, 629-638, 1976

Weiland, J. and Wilhelmsson, H.: Coherent Non-Linear Interaction of Waves in Plasmas, Pergamon, London, 1977.

Wait J. R.: Electromagnetic waves in stratified media, New York: IEEE Press and Oxford Univ. Press, 1996.

Wu, C.-C., Liou, K., Lepping, R. P., Hutting, L., Plunkett, S., Howard, R. A., Socker, D.: The first super geomagnetic storm of solar cycle 24: "The St. Patrick's day event (17 March 2015)", Earth, Planets and Space, 68, 151, https://doi.org/10.1186/s40623-016-0525-y, 2016.

Yiğit, E., Koucká Knížová, P., Georgieva, K., & Ward, W.: A review of vertical coupling in the Atmosphere–Ionosphere system: Effects of waves, sudden stratospheric warmings, space weather, and of solar activity, Solar-Terrestrial Physics, 141, 1–12, https://doi.org/10.1016/j.jastp.2016.02.011, 2016

Yu, Ya., Niu, J., Simpson, J. J.: A 3-D Global Earth-Ionosphere FDTD Model Including an Anisotropic Magnetized

966

967 **Appendix: the matrix coefficients included into eq. (16)**

968 Here the expressions of the matrix coefficients are presented that are used in the matrix factorization to compute the tensor

969 impedance, see eq. (16).

970
$$\hat{\alpha}_N^{(0)} = \begin{pmatrix} 1 + \dfrac{ih_z}{\Delta}(k_1 - \alpha_1\alpha_2 k_2); & \dfrac{ih_z}{\Delta}\alpha_2(k_2 - k_1) \\ \dfrac{ih_z}{\Delta}\alpha_1(k_1 - k_2); & 1 + \dfrac{ih_z}{\Delta}(k_2 - \alpha_1\alpha_2 k_1) \end{pmatrix}, \quad \hat{\alpha}_N^{(-)} = \begin{pmatrix} -1; & 0 \\ 0; & -1 \end{pmatrix}; \quad \Delta \equiv 1 - \alpha_1\alpha_2;$$

971
$$\hat{\alpha}_j^{(-)} = \begin{pmatrix} (\dfrac{\beta_{22}}{1 - \beta_{22}\frac{k_x^2}{k_0^2}})_{j-1/2}; & -(\dfrac{\beta_{21}}{1 - \beta_{22}\frac{k_x^2}{k_0^2}})_{j-1/2} + \dfrac{ik_x h_z}{2}(\dfrac{\beta_{23}}{1 - \beta_{22}\frac{k_x^2}{k_0^2}})_{j-1} \\ -(\dfrac{\beta_{12}}{1 - \beta_{22}\frac{k_x^2}{k_0^2}})_{j-1/2} + \dfrac{ik_x h_z}{2}(\dfrac{\beta_{32}}{1 - \beta_{22}\frac{k_x^2}{k_0^2}})_{j-1}; & (\beta_{11} + \dfrac{k_x^2}{k_0^2}\dfrac{\beta_{12}\cdot\beta_{21}}{1 - \beta_{22}\frac{k_x^2}{k_0^2}})_{j-1/2} - \dfrac{ik_x h_z}{2}(\beta_{13} + \dfrac{k_x^2}{k_0^2}\dfrac{\beta_{12}\cdot\beta_{23}}{1 - \beta_{22}\frac{k_x^2}{k_0^2}})_{j-1} - \\ & -\dfrac{ik_x h_z}{2}(\beta_{31} + \dfrac{k_x^2}{k_0^2}\dfrac{\beta_{32}\cdot\beta_{21}}{1 - \beta_{22}\frac{k_x^2}{k_0^2}})_{j} \end{pmatrix}$$

972
$$\hat{\alpha}_j^{(+)} = \begin{pmatrix} (\dfrac{\beta_{22}}{1 - \beta_{22}\frac{k_x^2}{k_0^2}})_{j+1/2}; & -(\dfrac{\beta_{21}}{1 - \beta_{22}\frac{k_x^2}{k_0^2}})_{j+1/2} - \dfrac{ik_x h_z}{2}(\dfrac{\beta_{23}}{1 - \beta_{22}\frac{k_x^2}{k_0^2}})_{j+1} \\ -(\dfrac{\beta_{12}}{1 - \beta_{22}\frac{k_x^2}{k_0^2}})_{j+1/2} - \dfrac{ik_x h_z}{2}(\dfrac{\beta_{32}}{1 - \beta_{22}\frac{k_x^2}{k_0^2}})_{j+1}; & (\beta_{11} + \dfrac{k_x^2}{k_0^2}\dfrac{\beta_{12}\cdot\beta_{21}}{1 - \beta_{22}\frac{k_x^2}{k_0^2}})_{j+1/2} + \dfrac{ik_x h_z}{2}(\beta_{13} + \dfrac{k_x^2}{k_0^2}\dfrac{\beta_{12}\cdot\beta_{23}}{1 - \beta_{22}\frac{k_x^2}{k_0^2}})_{j+1} + \\ & +\dfrac{ik_x h_z}{2}(\beta_{31} + \dfrac{k_x^2}{k_0^2}\dfrac{\beta_{32}\cdot\beta_{21}}{1 - \beta_{22}\frac{k_x^2}{k_0^2}})_{j} \end{pmatrix}$$

973

$$\hat{\alpha}_j^{(0)} = \left(\begin{array}{cc} -\left(\dfrac{\beta_{22}}{1-\beta_{22}\dfrac{k_x^{\,2}}{k_0^{\,2}}}\right)_{j-1/2} - \left(\dfrac{\beta_{22}}{1-\beta_{22}\dfrac{k_x^{\,2}}{k_0^{\,2}}}\right)_{j+1/2} + k_0^{\,2}h_z^{\,2}; & \left(\dfrac{\beta_{21}}{1-\beta_{22}\dfrac{k_x^{\,2}}{k_0^{\,2}}}\right)_{j-1/2} + \left(\dfrac{\beta_{21}}{1-\beta_{22}\dfrac{k_x^{\,2}}{k_0^{\,2}}}\right)_{j+1/2} \\[2em] \left(\dfrac{\beta_{12}}{1-\beta_{22}\dfrac{k_x^{\,2}}{k_0^{\,2}}}\right)_{j-1/2} + \left(\dfrac{\beta_{12}}{1-\beta_{22}\dfrac{k_x^{\,2}}{k_0^{\,2}}}\right)_{j+1/2}; & -\left(\beta_{11}+\dfrac{k_x^{\,2}}{k_0^{\,2}}\dfrac{\beta_{12}\cdot\beta_{21}}{1-\beta_{22}\dfrac{k_x^{\,2}}{k_0^{\,2}}}\right)_{j-1/2} - \left(\beta_{11}+\dfrac{k_x^{\,2}}{k_0^{\,2}}\dfrac{\beta_{12}\cdot\beta_{21}}{1-\beta_{22}\dfrac{k_x^{\,2}}{k_0^{\,2}}}\right)_{j+1/2} + \\[2em] & + k_0^{\,2}h_z^{\,2}\cdot\left(1-\beta_{33}\dfrac{k_x^{\,2}}{k_0^{\,2}}-\dfrac{k_x^{\,4}}{k_0^{\,4}}\dfrac{\beta_{23}\cdot\beta_{32}}{1-\beta_{22}\dfrac{k_x^{\,2}}{k_0^{\,2}}}\right)_{j} \end{array} \right).$$